Article

Typhoon-Induced Forest Damage Mapping in the Philippines Using Landsat and PlanetScope Images

Benjamin Jonah Perez Magallon [ID] and Satoshi Tsuyuki *[ID]

Department of Global Agricultural Sciences, Graduate School of Agriculture and Life Sciences, The University of Tokyo, Tokyo 113-8654, Japan; bpmagallon@g.ecc.u-tokyo.ac.jp
* Correspondence: tsuyuki@fr.a.u-tokyo.ac.jp

Abstract: Forests provide valuable resources for households in the Philippines, particularly in poor and upland communities. This makes forests an integral part of building resilient communities. This relationship became complex during extreme events such as typhoon occurrence as forests can be a contributor to the intensity and impact of disasters. However, little attention has been paid to forest cover losses due to typhoons during disaster assessments. In this study, forest damage caused by typhoons was measured using harmonic analysis of time series (HANTS) with Landsat-8 Operation Land Imager (OLI) images. The ΔHarmonic Vegetation Index was computed by calculating the difference between HANTS and the actual observed vegetation index value. This was used to identify damaged areas in the forest regions and create a damage map. To validate the reliability of the results, the resulting maps produced using ΔHarmonic VI were compared with the damage mapped from PlanetScope's high-resolution pre- and post-typhoon images. The method achieved an overall accuracy of 69.20%. The accuracy of the results was comparable to the traditional remote sensing techniques used in forest damage assessment, such as ΔVI and land cover change detection. To further the understanding of the relationship between forest and typhoon occurrence, the presence of time lag in the observations was investigated. Additionally, different contributing factors in forest damage were identified. Most of the forest damage observed was in forest areas with slopes facing the typhoon direction and in vulnerable areas such as near the coast and hill tops. This study will help the government and forest management sectors preserve forests, which will ultimately result in the development of a more resilient community, by making it easier to identify forest areas that are vulnerable to typhoon damage.

Keywords: typhoon-induced forest damages; harmonic series; forest monitoring; Google Earth Engine

1. Introduction

Forest conservation is essential to the economy of the Philippines and to reducing the impacts of natural disasters. Economically, forests provide valuable resources to the country as they contribute, together with agriculture and fisheries, to approximately 10% of the country's GDP [1]. Households, particularly poor and upland communities, depend highly on forest resources as their sources of income and daily use [2,3]. Communities with access to such resources have also experienced improvements in their socioeconomic status [4]. Thus, maintaining livelihoods while preserving forest cover is an important part of building a resilient community.

Relationships between forests and communities are complex during extreme events. Forests protect against small-scale events, such as rainfall; however, they could fall victim to disasters or become a contributor to the intensity and impact of the disaster [5]. Strong winds that uproot trees also frequently occur during powerful typhoons and flooding incidents, which exacerbates the damage. Moving after a disaster can be challenging due to roadblocks caused by trees left behind as debris. Forests also have little impact on reducing

flood peak flows in large-scale flooding events [6]. This makes proper forest management and planning for disasters essential but very challenging.

The Philippines' Leyte Region, which lies east of the Visayas Region, is one of the areas most frequently struck by typhoons. Over the past decade, the region has experienced multiple strong typhoons, including Typhoon Haiyan in 2013 and Typhoon Rai in 2021. These two typhoons were the costliest in the country's history, totaling approximately USD 3 billion in damage [7].

During such disasters, satellite data and remote sensing are indispensable tools for providing useful and timely information for disaster damage assessment. Finding the best vegetation index derived from satellite data to represent forest damage has been the focus of most studies. Aosier et al. [8] evaluated the area of fallen trees caused by Typhoon Songda in Hokkaido, Japan, by comparing the change (*ΔVI*) in NDVI, Leaf Area Index (LAI), and Normalized Difference Infrared Index (NDII) of the before- and after-typhoon images from ASTER. Their study found that the NDVI was a much more sensitive indicator than the NDII. By contrast, Wang et al. [9] compared five different vegetation indices' *ΔVI*s, NDVI, Enhanced Vegetation Index (EVI), NDII, LAI, and Fraction of Photosynthetically Active Radiation (Fpar), derived from MODIS data in assessing the damage caused by Hurricane Katrina at the De Soto National Forest in Mississippi, United States of America. They found that the NDII was the best damage indicator among the VIs. To determine the robustness of satellite-derived vegetation indices in monitoring typhoon-induced forest damage, Dong et al. [10] compared the effectiveness of the NDII and Disturbance Index (DI) as damage indicators by considering multiple typhoon events in Northeast China. They found that DI had better accuracy than NDII. Peereman et al. [11] attempted to reconcile these previous studies with other similar studies by assessing four different vegetation indices, NDVI, NDII, EVI, and the Soil-Adjusted Vegetation Index (SAVI), to measure canopy damage from five different typhoon occurrences in the Fushan Experimental Forest, Taiwan. They found that VI sensitivity varied in detecting typhoon-induced changes depending on canopy coverage and that there was no VI most sensitive to all typhoons. The authors suggested that a combination of different VIs should be used to evaluate typhoon-induced forest damage.

Machine learning (ML) has also been used in combination with remote sensing for such analyses. Zhang et al. [12] compared the reliability of the VI assessment method with the ML model random forest (RF) for measuring forest damage caused by Typhoon Rammasun in Guangdong and Hainan provinces in China in 2014. Their results showed that the VI method using NDII, NDVI, and EVI had a lower accuracy when compared to RF, with the highest difference of 7% and the lowest difference of 4% in overall accuracy (OA). Chen et al. [13] conducted a similar study by comparing the VI method with RF and Support Vector Machine (SVM) for their forest damage estimation using a three-typhoon occurrence event in 2016 in Hokkaido, Japan. RF and SVM performed better than VI, with a difference of 3% in OA for both models. Even though VI performed worse in comparison with ML in both studies, the difference was minimal considering the rigorous steps needed to be implemented in the ML.

Research on mapping and quantifying damage in forests is challenging because of the difficulty in obtaining accurate damage data for forests [14]. Analyzing historical data when evaluating forest damage brought on by disasters can help with this. It can provide context for the observed damages and, if integrated into the analysis and computations, could result in better estimations. This is particularly important in the Philippines, where different regions experience multiple typhoons annually.

Time lag is also an important factor when dealing with precipitation, as the response time for each vegetation type varies and is not immediately observable, as shown by Cui et al. [15] and Chuai et al. [16].

Satellite data, which is valuable, has some disadvantages. They suffer from noise and data gaps caused by external conditions, such as clouds, which are very frequent in regions such as the Philippines. One of the techniques that can address these gaps is harmonic

analysis of time series (HANTS). It has been used in various remote sensing applications. It has been used to model different attributes such as NDVI, Land Surface Temperature, and canopy cover [17–21]. It has also been used to measure forest responses to disturbances by relating these responses to changes in vegetation indices [22–24].

The aim of this study is to measure the impact caused by typhoons using remote sensing to fill the gaps in forest damage assessment research. The objectives were as follows: 1. Measure typhoon-induced forest damage. 2. Produce a forest typhoon-induced damage map that identifies damaged hotspots in the region. 3. Identify the presence of time lag and different factors related to forest damage. Through this, typhoon-susceptible forest regions in the province can be identified, which can help guide the government in developing appropriate forest management plans and typhoon responses for a more resilient forest and, in turn, build a more resilient community.

2. Materials and Methods

2.1. Materials

2.1.1. Study Area

The study area was the Leyte Region (Figure 1), located east of Visayas, Philippines (10.85° N, 124.85° E). It has a total area of approximately 7300 km^2 and a population of 2.6 million in 2020 [25]. It comprises two provinces, Leyte and Southern Leyte; 58 municipalities; and four cities. Situated close to the Pacific Ocean, the region is bordered to the east by Samar Island and the Leyte Gulf, to the west by the Camotes Sea, and to the north by Biliran Island. Its topography is flat along coastal areas with mountainous interiors. The forests in this region are dominated by evergreen and semi-deciduous trees [26].
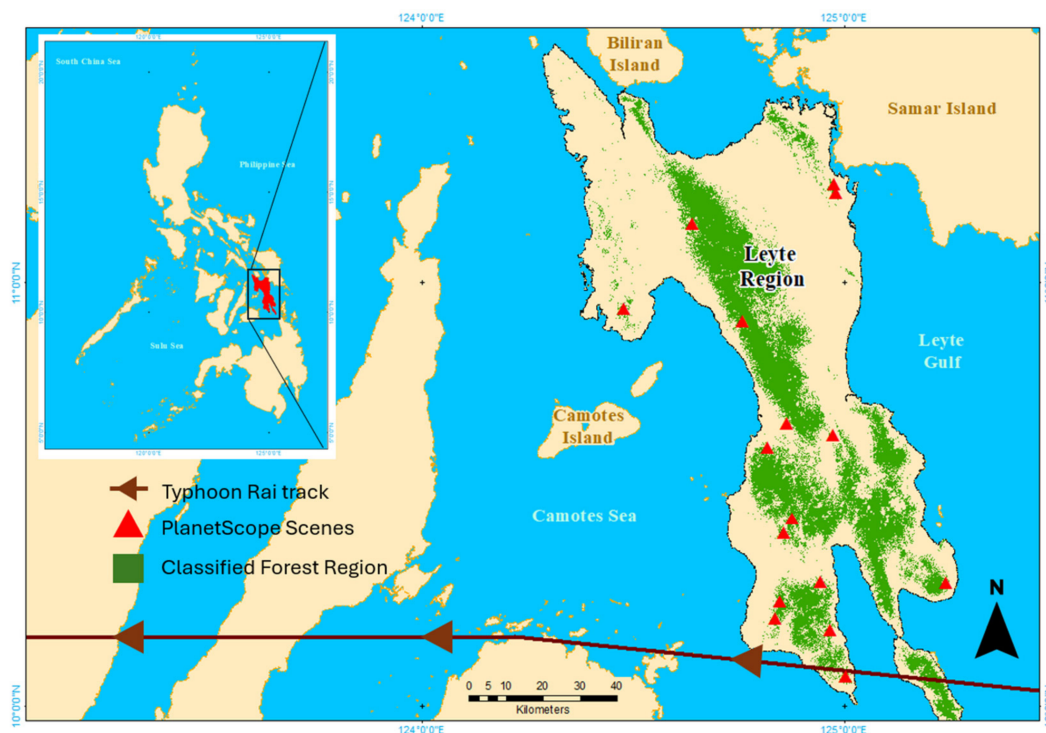
Figure 1. Leyte Region (black line), overlayed with the classified forest regions (green), validation scenes (red triangle), and typhoon Rai ground track (brown line) (add north arrow).

2.1.2. Typhoon Rai

On 14 December 2021, Typhoon Rai, also known as Super Typhoon Odette in the Philippines, made landfall in the Philippine Area of Responsibility (PAR) and was classified as a severe tropical storm with a maximum sustained wind speed of 100 km/h and a pressure of 985 hPa [27]. The typhoon intensified to a Super Typhoon, reaching a wind

speed of 280 km/h as it made landfall in the Southern Philippines. It caused severe and widespread damage across multiple regions in the country, costing approximately USD 1.02 billion in damages, the 2nd costliest typhoon in history. The typhoon left the PAR on December 18, displacing thousands of families and causing approximately 400 deaths [28]. The typhoon paths relative to the study area are shown in Figure 1.

2.1.3. Satellite Data
Landsat-8

The Landsat-8 Satellite was launched on *11 February 2013*. The system was equipped with the Operational Land Imager (OLI), composed of six multispectral bands ranging from blue to shortwave infrared bands with a spatial resolution of 30 m. The satellite covers an area of 185 × 180 km per scene and has a temporal resolution of 16 d [29].

In this study, Landsat-8 OLI Surface reflectance (SR) images from the Google Earth Engine (GEE) were used as the main source of information for analysis. The dataset has a wide temporal range, starting from 2013 to present. This would help in the better estimation of undisturbed phenology needed in this study as it would give more samples through different times. Moreover, Typhoon Haiyan, a typhoon with the same category as Typhoon Rai, passed over the region in 2013. Using Landsat would let the event be included in building HANTS and make the method more representative of the extreme events that occurred in the region. The boundary utilized for processing the Landsat data in the GEE was the Leyte Region, as depicted in Figure 1.

PlanetScope

PlanetScope is a constellation of more than 430 Dove and SuperDove satellites that can cover the entire Earth daily [30]. Its images have a spatial resolution of 3–4.1 m and spectral bands ranging from blue to near-infrared. Each scene has an approximate area of 280–360 km^2 depending on the type of instrument used in the imaging [31].

PlanetScope images have been widely used by different studies for forest change detection application due to its high temporal resolution and high spatial resolution [32–37]. In this study, subsets of PlanetScope images were used to build validation data through visual interpretation to map the changes in the region before and after the typhoon. The distribution of the images used is shown as red triangles in Figure 1. The city and municipality where each scene was located, together with its coverage area, are listed in Table 1.

Table 1. PlanetScope scenes used for validation.

Location	Acquisition Dates (Pre- and Post Typhoon)	Area (km^2)
Albuera	4 December 2021, 12 January 2022	30.08
Baybay City	20 November 2021, 10 January 2022	17.55
Hilongos	20 November and 12 December 2021, 12 January 2022	48.86
Hindang	20 November 2021, 12 January 2022	30.91
Isabel	4 December 2021, 6 January 2022	7.18
Maasin City	25 October 2021, 19 December 2021	9.13
Matalom	20 and 23 November 2021, 8 January 2022	18.68
Mahaplag	21 October 2021, 24 December 2021	7.50
Malitbog	4 December 2021, 11 January 2022	6.20
Ormoc City/Kananga	1 December 2021, 6 January 2022	49.98
Padre Burgos	4 December 2021, 11 January 2022	31.55
San Juan	4 December 2021, 10 January 2022	14.32
Tacloban City (2 sites)	23 November 2021, 23 December 2021	16.45
Tomas Oppus	20 November 2021, 10 January 2022	23.28
Total Area:		311.67

2.1.4. Topographic Data

The elevation, slope, and aspect data used in this study were derived from the Advanced Land Observing Satellite (ALOS) digital surface model (DSM) global dataset with an approximate resolution of 30 m [38]. Data were acquired throughout ALOS's operational lifetime from 2006 to 2011.

All the data and its derivatives used in this study are listed in Table 2.

Table 2. List of data used in this study.

Data	Spatial Resolution	Derived Data	Temporal Range
Satellite Data			
Landsat-8 OLI SR [28]	30 m	Landsat-8 Composite Image	7, 16, and 23 April 2, 9, 18, and 25 May 3 and 19 June 12, 21, and 28 July 2020
		Forest Cover Map	2020
		Monthly Land Cover Map 2021–2022	November 2021–February 2022
		Forest Damage Map from LCC	November 2021–December 2021, November 2021–January 2022, November 2021–February 2022
		Monthly Landsat-derived VI and HANTS VI	2013–2022
PlanetScope [29]	3–4.1 m	Forest Pre- and Post-Change Detection Map	See Table 2.
Forest Data			
NAMRIA Land Cover Map of Leyte Region, 2020 [39,40]		Training points for Land Classification	
Sentinel-1		VV and VH Median	April–July 2020
Topographic Data			
ALOS DSM [38]	30 m	Elevation, Slope, Aspect	
Typhoon Rai ground track [27]		Forest Damage Proximity Map	

2.2. Methods

The workflow of this study is illustrated in Figure 2. This can be summarized in three steps. First, the degree of harmonics best fitted to this study was identified by comparing the 1st-, 3rd-, and 6th-degree *ΔHarmonic VI* to the validation data. At the same time, the most sensitive VI in terms of typhoon-induced forest damage was identified. The result from the first step was used to create a Forest Damage Map. Second, the accuracy of *ΔHarmonic VI* was compared to those of the traditional methods ΔVI and LCC. Lastly, time lag was investigated and the topography and typhoon track were related to the map.

2.2.1. Data Preprocessing

In order to perform the necessary analyses in this study, several data preprocessing steps were carried out to the Landsat and PlanetScope images, ALOS, and Typhoon Track. Derivative data such as the Forest Land Cover Map and Land Cover Change Map were also produced. The former was used as the reference forest area for all the analyses, while the latter was used for comparison to this study's proposed method.
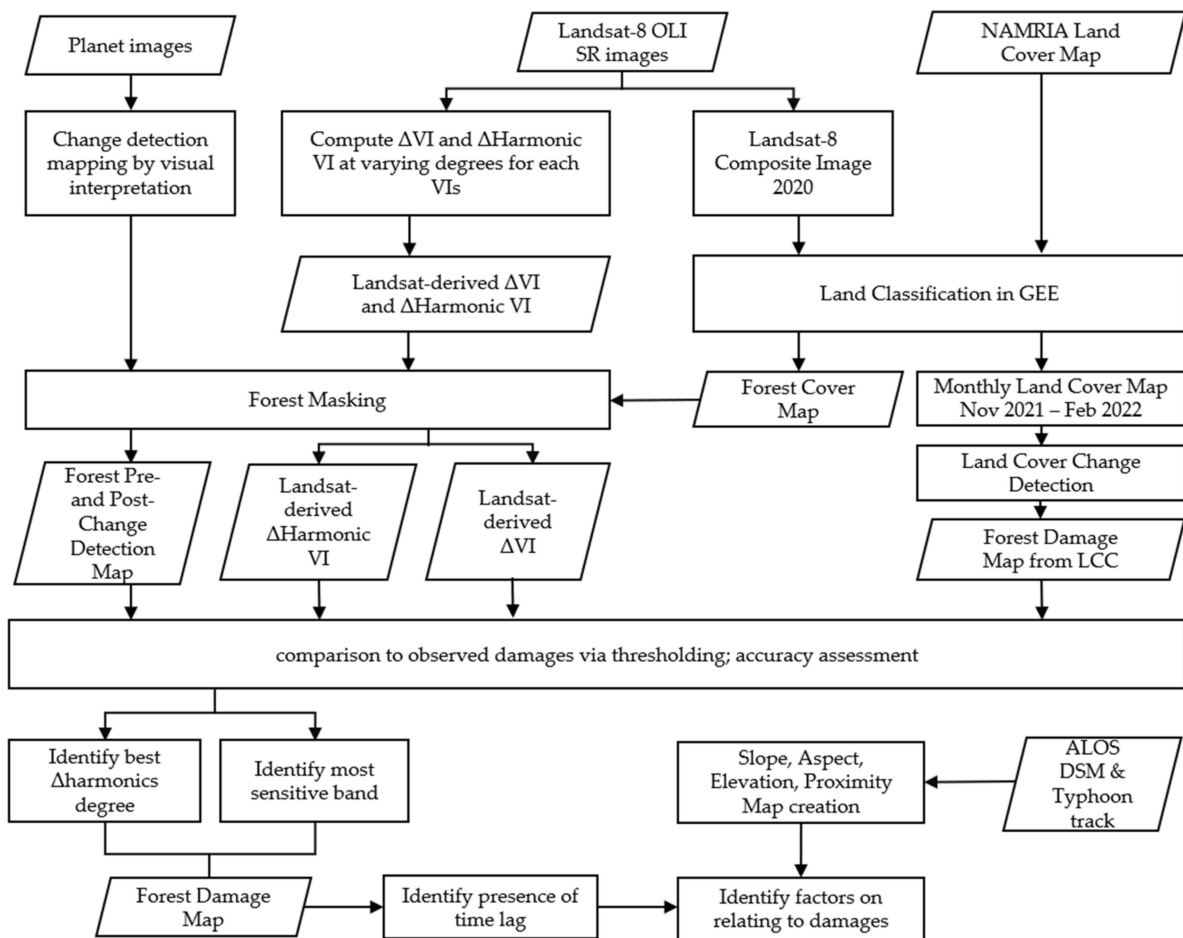
Figure 2. Workflow of this study.

Landsat

Three sets of Landsat-8 images were generated using GEE. The first was a Landsat-8 composite image of the Leyte Region for the year 2020 using images taken on 7, 16, and 23 April; 2, 9, 18, and 25 May; 3 and 19 June; and 12, 21, and 28 July 2020. The composite was made by first calculating the maximum NDVI across all of the images, and then choosing the pixels for each Landsat band composite based on the maximum NDVI. The composite image was used for land-cover classification using random forest to create a forest cover map of the region. The second set of images was a monthly land cover (LC) map from November 2021 to February 2022. Each image was derived from the median monthly Landsat image for the region. The median was used to reduce noise in the data as it has shown to be robust to outliers [24,41]. The monthly LC was used for land cover change detection to create a Forest Damage Map. They were classified using the same model classifier as that used for the composite images. Lastly, the monthly Landsat-derived VI and HANTS VI were produced from the median monthly Landsat image for the region. The latter was an output from harmonic series of the median monthly images. It was used in computing ΔHarmonics VI and for comparative analysis. In order to account for lag time effects, images were created in December 2021 and in January and February 2022.

PlanetScope

PlanetScope's before- and after-typhoon images were used to create two classes in the validation data: forest and forest loss. By contrasting the damage seen prior to and following the typhoon, the extent of the forest loss was determined. The forest class, on the other hand, was delineated by extracting the remaining areas in the scene that were not covered by the delineated damaged areas and were intersected with the created forest

cover map using Landsat data. Figure A1 presents an example of the validation dataset used in this study.

Forest Cover Map

The forest cover used in this study was derived from the created composite Landsat image and using National Mapping and Resource Information Authority's (NAMRIA) 2020 LC Map of Region 8, Philippines [39], as the training data through random forest classification in GEE. The NAMRIA LC Map was digitally interpreted from the 2019–2020 Sentinel-2 satellite 10 m resolution imagery. The Open and Closed Forest classes in the LC Map [40] were grouped as forest, and the remaining classes were grouped as non-forest. The training points were generated from the LC map and applied to the 2020 Landsat-8 Composite Image of the Leyte Region.

The median of the Sentinel-1 SAR data (VV and VH) from April to July 2020, ALOS DSM (elevation, slope, and aspect), and vegetation indices NDVI and NDWI from Landsat-8 over the Leyte Region were added as additional layers in the classification analysis. The final map, which has an overall classification accuracy of 85%, is displayed in Figure 1. This forest cover map was used as a base reference for forest coverage in all analyses performed in this study.

The GEE code used to create the composite and forest cover maps of the Leyte Region can be found at https://code.earthengine.google.com/82da315e4a8cf530b64d747387ac31dc (accessed on 29 March 2024).

Land Cover Change Map

Three Land Cover Change (LCC) Maps were created by comparing the pre-typhoon November 2021 LC Map with the post-typhoon December 2021, January 2022, and February 2022 LC Maps.

The LCC was derived by merging the cloud covers of each monthly LC map. Each LC map was then masked using the merged cloud cover. This was performed to ensure that each of the LC maps had similar coverage and was comparable to each other.

After masking, the LC maps were paired. The pairs were November 2021–December 2021, November 2021–January 2022, and November 2021–February 2022. For LCC detection, post-typhoon forest cover was subtracted from pre-typhoon forest cover for each LC map pair. This difference represents forest loss for each pair. Finally, to create a Forest Damage Map from the LCC, the forest loss from the difference was mosaicked onto the forest cover of the post-typhoon period for each pair.

Forest Damage Proximity Map

To relate the Typhoon Rai ground track to the Forest Damage Map, a Forest Damage Proximity Map was created by measuring the perpendicular distance (m) between each forest damage pixel and the typhoon track.

2.2.2. Determining the Best Harmonic Degree and VI
Vegetation Indices

To successfully measure typhoon-induced forest damage, there is a need to identify which vegetation index is the most sensitive to such change. The vegetation indices considered in this study that could best represent the forest response to typhoons were the Normalized Difference Vegetation Index (NDVI), Enhanced Vegetation Index (EVI), Normalized Difference Infrared Index (NDII), and Green-Red Vegetation Index (GRVI).

The Landsat-8 images contain five bands that can be used to derive all vegetation indices: blue (B), red (R), green (G), near-infrared (NIR), and first shortwave infrared (SWIR1).

The NDVI is a widely used metric in remote sensing for assessing vegetation health and vigor and can be computed using Equation (1).

$$NDVI = \frac{(NIR - R)}{(NIR + R)} \tag{1}$$

NDVI has been used for forest damage detection by comparing changes in NDVI values over time [42,43]. However, the index saturates for highly dense vegetation compared to other VIs [44].

EVI, on the other hand, is more sensitive to dense vegetation than NDVI and has been used to evaluate vegetation health [44–46]. This index can be computed using Equation (2). The atmospheric adjustments and canopy background are represented by the constants in the equation.

$$EVI = 2.5 \times \left(\frac{NIR - R}{NIR + 6 \times R - 7.5 \times B + 1} \right) \tag{2}$$

The NDII is another vegetation index derived from remote sensing data that can be valuable for forest damage assessment, particularly for assessing water stress within vegetation. This index can be calculated using Equation (3).

$$NDII = \frac{NIR - SWIR1}{NIR + SWIR1} \tag{3}$$

A study by Wang et al. [9] showed that NDII has a much higher sensitivity than NDVI and EVI in assessing forest damage caused by Hurricane Katrina. Other studies have shown that NDII provides a better monitoring of canopy and forest structural changes [47,48].

Finally, the GRVI is typically used to detect changes in vegetation phenology. This index can be computed using Equation (4).

$$GRVI = \frac{G - R}{G + R} \tag{4}$$

Motohka et al. [49] used this index to detect the early phase of leaf green-up and the middle phase of autumn, when leaf yellowing occurs. They also noted that the index could be used to detect disturbances such as typhoon occurrences in vegetation.

Although these VIs offer valuable insights into forest monitoring, it is important to consider their limitations, including sensitivity to atmospheric conditions, soil properties, and sensor characteristics. Thus, in this study, these VIs were used together with HANTS and evaluated together with ΔVI, LCC observed in Landsat, and validation data from PlanetScope images.

Decomposing VI Values to Map Typhoon-Induced Forest Damage through HANTS

The signal observed by a satellite from a particular pixel in an image is composed of different sources, such as vegetation growth, seasonal variation, and/or other disturbances. When applied pixel-by-pixel, Harmonic Analysis on Time Series (HANTS) can decompose this signal into the sum of constant and cosine functions with different frequencies by taking into account the most important frequencies in the signal's historical data and using a least-squares curve fitting procedure based on harmonic components. Equation (5) shows the underlying function of HANTS for a given temporal N observation of y from $i = 1$ to N [50,51].

$$y(t) = a_0 + \sum_{i=1}^{M} a_i \, cos(\omega_i t_i - \theta_i) \tag{5}$$

The constant a_0 is the mean of all N observations of y. M is the number of frequencies in the series, where M $\leq$ N. In this study, M refers to the degree of harmonics. ω_i is the frequency of the ith harmonic term and t_i is the time when the ith sample was taken. a_i and θ_i represent the amplitude and the phase of the ith harmonic term, respectively.

The amplitude and phase of the cosine function in Equation (5) are determined through an iterative fitting process for each harmonic. Initially, a least-squares curve is generated using all data points within the valid range. This curve is then compared with the observation points, and any points that significantly deviate from the fitted curve are identified and removed. The process is repeated until no points exceed the predefined error threshold.

In this study, a harmonic-fitted curve was assumed to be the ideal representation of the undisturbed phenology based on previous studies [17–24]. HANTS was used to compute *ΔHarmonic VI*, whose formula is shown in Equation (6). *ΔHarmonic VI* is the percentage change between the actual observed VI value of the forest and *HANTS VI*, which represents the undisturbed forest phenology or the ideal VI value of the forest without typhoons. The *Con* in *the equation* is a conditional expression, where if "*HANTS VI < 0*" is true, a −1 value will be multiplied by *the equation*, or 1 if it is false.

As previously stated, HANTS can decompose a signal from a pixel. When considering a signal from a forest pixel, HANTS decomposes it into different components, such as vegetation growth, seasonal variation, and disturbances. *ΔHarmonic VI* seeks to obtain the signal of any disturbance from these other signals by subtracting the undisturbed forest signal, *HANTS VI*, from the *Observed VI* which contains all the forest signals, including typhoon disturbances, using Equation (6). *HANTS VI* is a simulated VI image on the same date as *Observed VI*.

The HANTS was implemented using GEE, similar to that used by Philipp et al. [24] when they applied HANTS to measure drought effects on German forests.

$$\Delta Harmonic\ VI = \left(\frac{Observed\ VI - HANTS\ VI}{HANTS\ VI} \right) \times 100 \times Con(HANTS\ VI < 0, -1, 1) \quad (6)$$

The key parameter for obtaining forest disturbance signals through HANTS is the number of frequencies considered in the series, or the degree of harmonics. This pertains to the number of signals considered in the HANTS. The goal of this study was to determine the degree of harmonics that best represents the ideal phenology of the study area. To determine the degree, the 1st, 3rd, and 6th degrees of all the ΔHarmonics VIs were considered. Usually, ideal vegetation phenology can be explained by the first three degrees [22–24], which are from vegetation growth and seasonal variation; thus, the 1st and 3rd degrees were considered. In order to account for the potential existence of disturbances other than typhoons, such as atmospheric and local disturbances, the 6th degree was included in the analysis. This was also employed to make up for any potential spectral mixing brought on by the data's spatial resolution [23].

Separating Forest With and Without Loss through Thresholding

To make the *ΔHarmonic VI* comparable to the observed change in the validation data, each *ΔHarmonic VI* pixel for all VIs considered was divided into two groups in terms of the percentage change in each pixel value. The two groups were as follows: no loss, which are pixels with a percentage change greater than a set threshold, and with loss, which are pixels with a percentage change less than a set threshold.

Instead of using negative values to classify areas with forest cover loss, thresholding was performed to compensate for changes in the area such as partial forest regrowth, different sensitivities for each harmonic degree and VIs, and time-lag effects. The same approach has been used in previous studies, such as those by Furukawa et al. [52] and Chen et al. [13].

A threshold that best fits each VI was set by computing the accuracy of each *ΔHarmonic VI* at varying thresholds, ranging from −5% to −100% changes at a −5% change interval. A −5% threshold indicates that the forest loss value considered ranges from −5% to a lower percentage change in the VI. Thus, the lower the threshold value, the narrower the range of percentage change in VIs, considering forest loss. As for the 0–5% measured change, the highest threshold of −5% was chosen to account for potential system and image errors [24,26]. The −100% lowest threshold was set to represent the complete change in land cover, where forest cover before the typhoon changed to barren soil after. Thresholding was performed to determine the threshold value for each VI that best separates forests with and without loss. The sensitivity of each VI type was also investigated.

By comparing the threshold values for each harmonic degree, it was possible to determine which VI was most sensitive to forest damage. High threshold values show less

sensitivity, as it is necessary to consider wider ranges of negative percentage change in VIs to detect forest-loss areas, whereas low threshold values show otherwise. To consider time-lag effects, December 2021, January 2022, and February 2022 were considered as *Observed VI* in computing the *ΔHarmonic VI* in all of the analyses.

2.2.3. Accuracy Assessment and Validation

The validation metrics used in this study were as follows: each *ΔHarmonic VI* accuracy when compared to the validation data computed through a confusion matrix (1000 points created from equalized stratified random sampling were generated for each assessment of *ΔHarmonic VI*); and the OA, which is the average accuracy per degree of *ΔHarmonic VI* for the 3 months: December, January, and February. The sampling method was selected to represent the two classes equally.

The resulting accuracy of each ΔHarmonic VI was further compared to the accuracy of the usual forest damage assessment methods, *ΔVI* and LCC. *The equation* used for *ΔVI* is shown in Equation (7). The steps for forest loss delineation in *ΔVI* were the same as the steps performed for delineation in *ΔHarmonic VI* for all of the VIs.

$$\Delta VI = \left(\frac{PostTyphoon\ VI - PreTyphoon\ VI}{PreTyphoon\ VI} \right) \times 100 \times Con(PreTyphoon\ VI < 0, -1, 1) \quad (7)$$

By performing these comparisons, the reliability and accuracy of *Δ*Harmonic VI and the soundness of the assumption that the difference represents the actual change in vegetation and typhoon disturbances can be confirmed.

2.2.4. Creating Forest Damage Map

Using the best degree and most sensitive VI in computing *ΔHarmonic VI*, a damage map that could best represent the typhoon-induced damages was created. Section 2.2.2's delineation method was used to identify the areas that sustained damage from the typhoon. In order to assist the government in disaster response and appropriate rehabilitation planning, hotspots for forest loss and typhoon-vulnerable areas were identified. To see the difference and advantage of using *ΔHarmonic VI*, the created map was compared side by side with the damage map derived from *ΔVI* and the LCC map as well.

2.2.5. Investigating the Presence of Time Lag

Accounting for the time lag is crucial in the analysis using different VIs as indicators of changes in forest phenology, as shown in previous studies [15,16]. The lag can vary depending on factors, such as vegetation cover, climate, and other environmental conditions. Different vegetation types respond differently to environmental changes. Some may show immediate responses, whereas others may show delayed or cumulative responses. It can also vary depending on the VI used.

To determine the presence of time lag in this study, the pixel count for forest and forest loss from December 2021 to February 2022 of the three best performing *ΔHarmonic VI* were tabulated to check the trend in the two classes.

2.2.6. Determining Contributing Factors to Forest Damage

To further understand the measured forest damage and the dynamics between the forest, its terrain, and typhoons, the Forest Damage Map was matched with the Forest Damage Proximity Map, elevation, slope, and aspect.

This was implemented by overlaying the Forest Damage Map on the topography and proximity map to relate the forest loss areas to the terrain layers, which are the distance to the typhoon, elevation, slope, and aspects derived from the Typhoon Rai track and the ALOS DSM.

To ascertain which topographic features contributed to forest damage, the observable trends for each comparison of forest loss observed with those features were examined.

3. Results

3.1. Determing the Best Harmonic Degree and VI

3.1.1. Thresholding

Figure 3 shows the result of the OA of each *ΔHarmonic VI* for every set threshold. The general trend for all VIs was that the OA increased slightly as the threshold increased. The NDVI (Figure 3a) had its highest peak in OA at 67.20%, the NDII (Figure 3b) at 69.10%, the EVI (Figure 3c) at 69.20%, and the GRVI (Figure 3d) at 65.60%. This relatively flat trend can be explained by checking the producer's accuracy (PA) of the EVI for forests with and without loss, as shown in Figure 4. The EVI was selected because it had the highest OA peak among the *ΔHarmonic VI*s. The PA of the no-loss areas (Figure 4a) increased as the threshold increased; however, the PA of the loss areas (Figure 4b) decreased as the threshold increased. The observed opposite trends balanced the effect of using multiple thresholds, resulting in a flatter OA trend. The low PA of no-loss areas was expected since *ΔHarmonic VI*, continuous data, gives information about the changes in remaining forest covers as well. Subtle changes in the VI were categorized as forest losses, so higher thresholds tended to underestimate forests that were not lost.
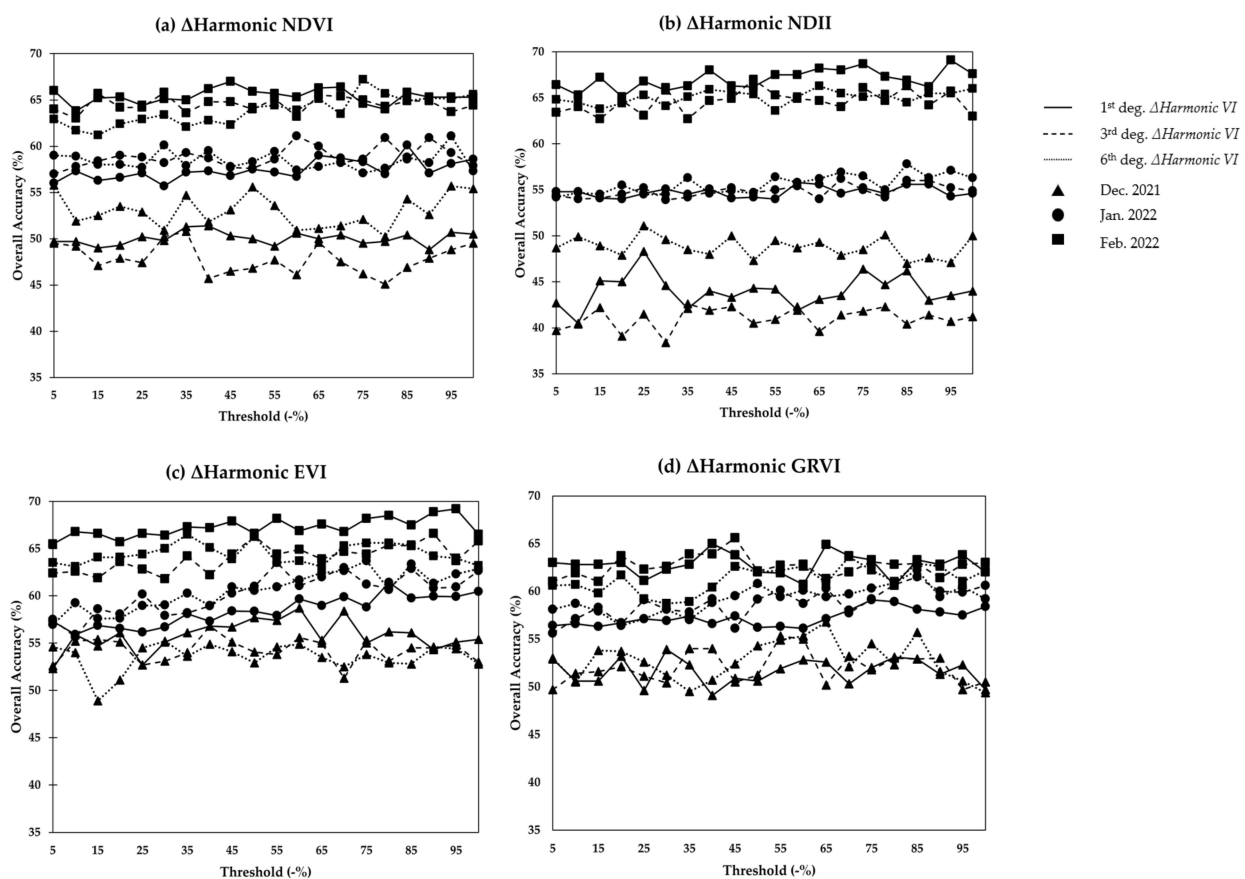
Figure 3. Overall accuracy at varying thresholds for each ΔHarmonic: (**a**) NDVI, (**b**) NDII, (**c**) EVI, and (**d**) GRVI.

The 1st degree of all *ΔHarmonic VI*s performed better overall than the 3rd- and 6th-degree *ΔHarmonic*. The highest was measured at the 1st degree of *ΔHarmonic* EVI with an OA of 69.20%, followed by the 1st degree of *ΔHarmonic* NDII with an OA of 69.10%, both in the month of February.
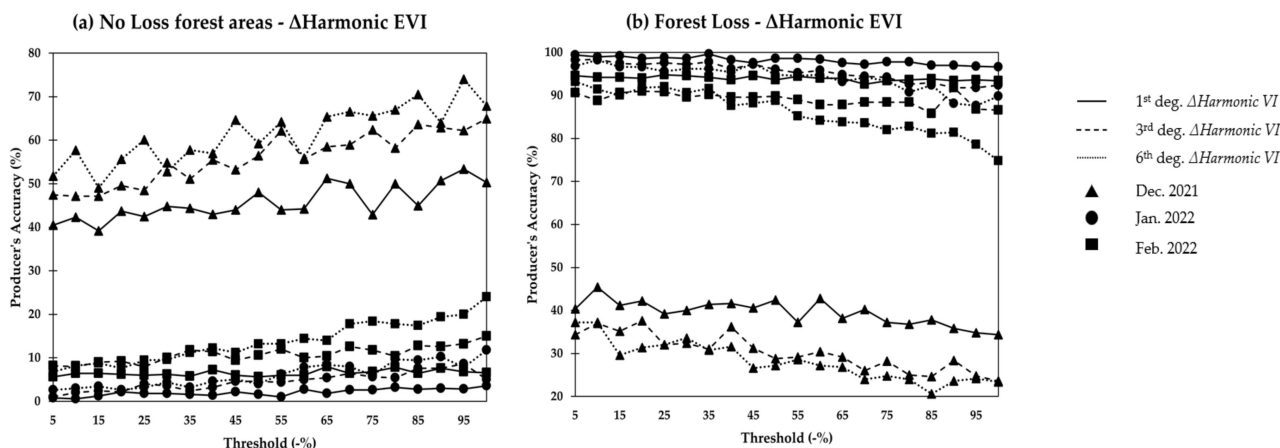
Figure 4. Producer's accuracy at varying thresholds for ΔHarmonic EVI: (**a**) no loss, and (**b**) loss.

The *ΔHarmonic VI* in the month of February had the best OA, as all of the OA peaks for each degree and VI were observed in this month. December exhibited the worst performance across all of the degrees and VIs. This difference was evident in the NDII and was much closer in the EVI and GRVI plots. The underperformance was due to the timing of the typhoon occurrence (14 December), which took place in the middle of December. The December monthly images comprised 6 and 22 December Landsat-8 OLI SR images. The presence of pre-typhoon (6 December) measurements affected the OA for the month. As all forest losses were visible in the February data, the dates for which post-typhoon images were used to construct the validation data fall between December and January. As time goes on, the measured damage from the VIs becomes more noticeable, which is another reason for the variation in months.

For NDVI (Figure 3a), the OA of the 1st degree of *ΔHarmonic* peaked at 67% using a −45% threshold, the 3rd degree of *ΔHarmonic* peaked at 65.80% applying a −30% threshold, and lastly, the 6th degree of *ΔHarmonic* peaked at 67.20% with a −75% threshold.

For NDII (Figure 3b), the OA of the 1st degree of *ΔHarmonic* peaked at 69.10% using a −95% threshold, the 3rd degree of *ΔHarmonic* peaked at 67.00% applying a −50% threshold, and lastly, the 6th degree of *ΔHarmonic* peaked at 66.30% with a −65% threshold.

For EVI (Figure 3c), the OA of the 1st degree of *ΔHarmonic* peaked at 69.20% using a −95% threshold, the 3rd degree of *ΔHarmonic* peaked at 66.60% applying a −90% threshold, and lastly, the 6th degree of *ΔHarmonic* peaked at 66.50% with a −35% threshold.

Lastly, for GRVI (Figure 3d), the OA of the 1st degree of *ΔHarmonic* peaked at 65.00% using a −40% threshold, the 3rd degree of *ΔHarmonic* peaked at 65.60% applying a −45% threshold, and lastly, the 6th degree of *ΔHarmonic* peaked at 63.60% with a −70% threshold.

Judging by each VI peak at different degrees, NDVI and GRVI showed less sensitivity to damage compared to NDII and EVI, as both the former needed higher thresholds to accurately map the damage.

Figure 5 shows the OA results for each *ΔVI* at varying thresholds. Similar to the trend observed in the *ΔHarmonic VI* plots, the general trend observed in *ΔVI* is relatively flat aside from some sudden rises and dips in some trends. The highest OA for *ΔVI* was 67.60% observed at NDVI, followed by 66.57% for EVI and 64.90% for NDII. To give context to its trend, the PA of ΔEVI for forest areas with and without loss is shown in Figure 6. ΔEVI was selected to make the trend in *ΔVI*'s PA comparable to *ΔHarmonic VI*'s PA (Figure 4) by showing the same VI. Figure 6a,b show the opposite trend with increasing thresholds, similar to *ΔHarmonic VI*, resulting in a flat OA trend.
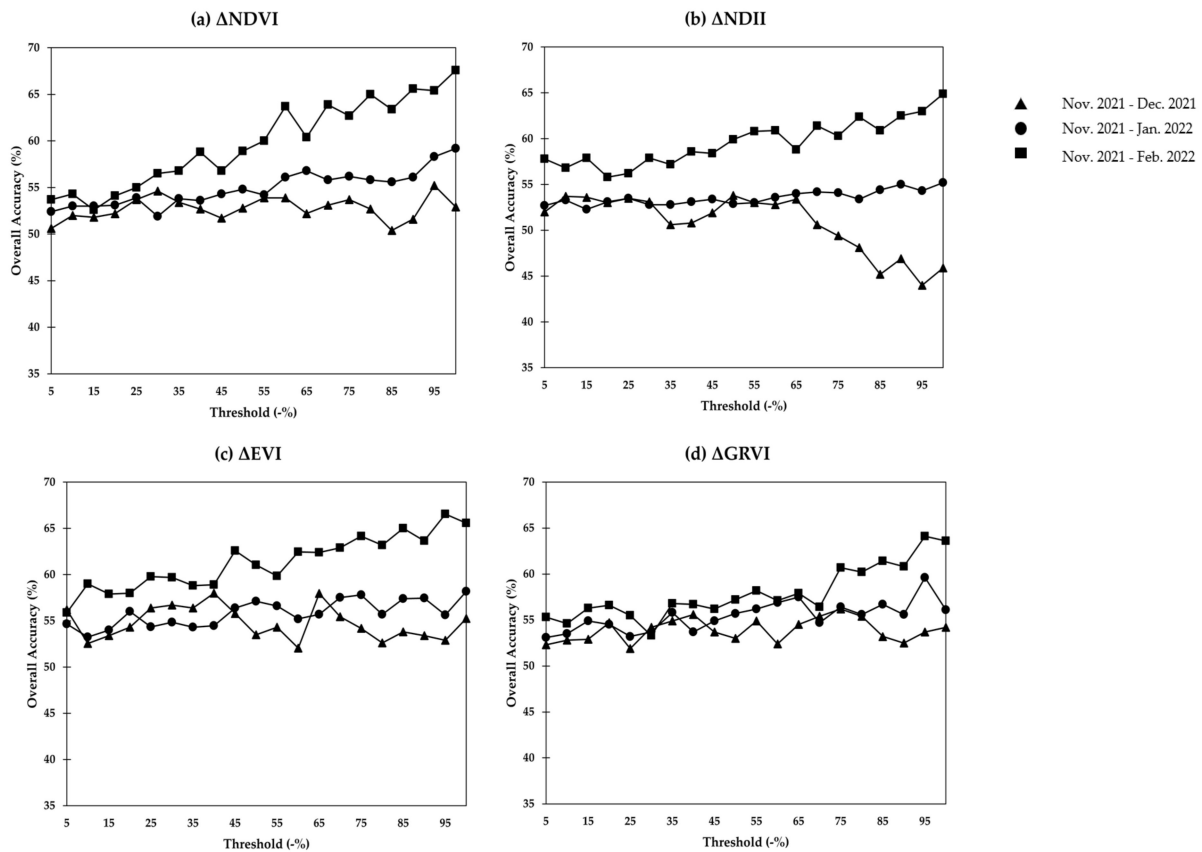
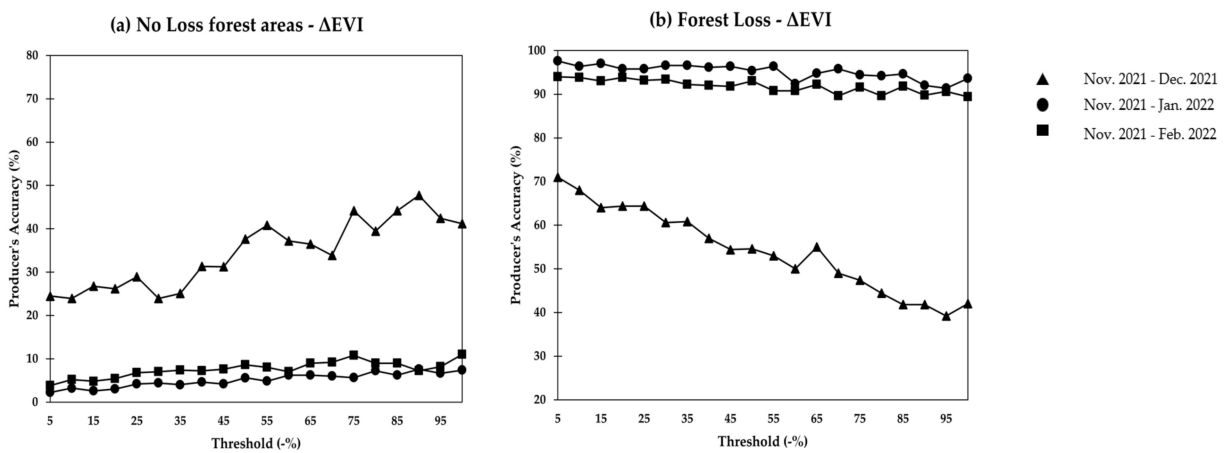**Figure 5.** Overall accuracy at varying thresholds for each *ΔVI*: (**a**) NDVI, (**b**) NDII, (**c**) EVI, and (**d**) GRVI.

Figure 6. Producer's accuracy at varying thresholds for ΔEVI: (**a**) no loss, and (**b**) loss.

3.1.2. Comparison of *ΔHarmonic VI* to *ΔVI* and LCC

The highest OA of each degree of *ΔHarmonic VI* with its corresponding threshold is shown in Figure 7. The highest accuracy observed was the 1st-degree ΔHarmonic EVI, with an accuracy of 69.20% using a −95% threshold, followed by the 1st-degree ΔHarmonic NDII with an accuracy of 69.10% applying a −95% threshold and 6th-degree ΔHarmonic NDVI with an accuracy of 67.20% with a −75% threshold, all in the month of February.
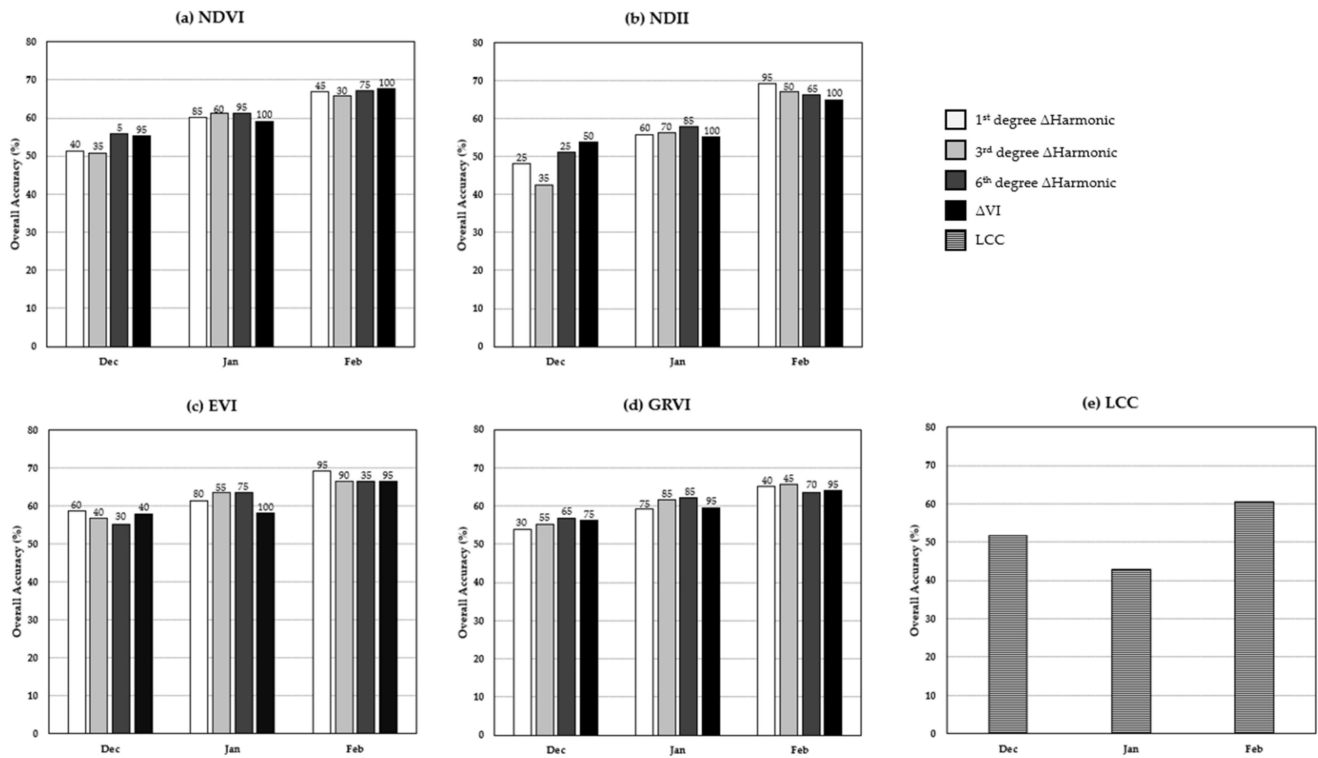
Figure 7. Overall accuracies of 1st-, 3rd-, and 6th-degree harmonic and *ΔVI* for each VIs: (**a**) NDVI, (**b**) NDII, (**c**) EVI, and (**d**) GRVI; and accuracy of forest cover loss from (**e**) LCC detection. The numerical value on the top of each bar indicates its threshold value.

The best degree on each ΔHarmonic VI was the 1st degree. The 6th-degree harmonic had the lowest accuracy for almost all the VIs; however, the difference was small. The largest difference observed was at 2.80% in ΔHarmonic NDII, and the smallest difference observed was at −0.2% in ΔHarmonic NDVI.

The degree and VI with the best OA, considering 3 months for the time lag, were the 1st degree of ΔHarmonic EVI, with an average OA of 63.10%. It also had the highest peak among the VIs, and its thresholds were lower, showing high sensitivity to forest loss. Thus, EVI is the best VI for assessing typhoon-induced damage to forest cover in the Leyte Region. The NDII is also a good VI for forest loss assessment, as it has the 2nd highest peak among the VIs and shows high sensitivity to forest loss, as well as low threshold values.

The performance of *ΔHarmonic VI* was comparable to the performance of *ΔVI* and LCC accuracy. The highest accuracy observed for *ΔVI* was ΔNDVI between November 2021 and February 2022, with an accuracy of 67.60%, and the highest OA, considering the three month-to-month comparisons, was 60.91% observed in ΔEVI. The lowest accuracy observed for *ΔVI* was ΔNDII between November 2021 and January 2022 with an accuracy of 53.80%, and the lowest average OA considering the three month-to-month comparisons was ΔNDII at 57.97%. The NDII performed poorly in December for both *ΔHarmonic VI* and *ΔVI*, which can be attributed to the effect of the presence of pre-typhoon data, as discussed in Section 3.1.1., and a high sensitivity to forest loss.

The LCC had the highest accuracy of 60.60% observed in November 2021 and February 2022, in the before- and after-typhoon images. With an accuracy of 43.00%, the period from November 2021 to January 2022 was the least accurate. LCC's average OA was 51.73%. Due to its underestimation of the areas experiencing forest loss, LCC performed poorly. This was evident in the high error of omission of forest loss areas at 49.60% and the very low error of forests with no-loss areas at 29.20%. The sampling method did not help the LCC either, as it gave the same weight to both forests, with and without loss classes.

3.2. Creating Forest Damage Map

The first-degree ΔHarmonic EVI using data from February 2022 was found to be the most sensitive to typhoon-induced damage, with an OA of 69.20% throughout the 3-month period from December 2021 to February 2022. Using this, a damage map of forest cover in the Leyte Region was generated and is shown together with the ΔEVI and LCC maps in Figure 8.
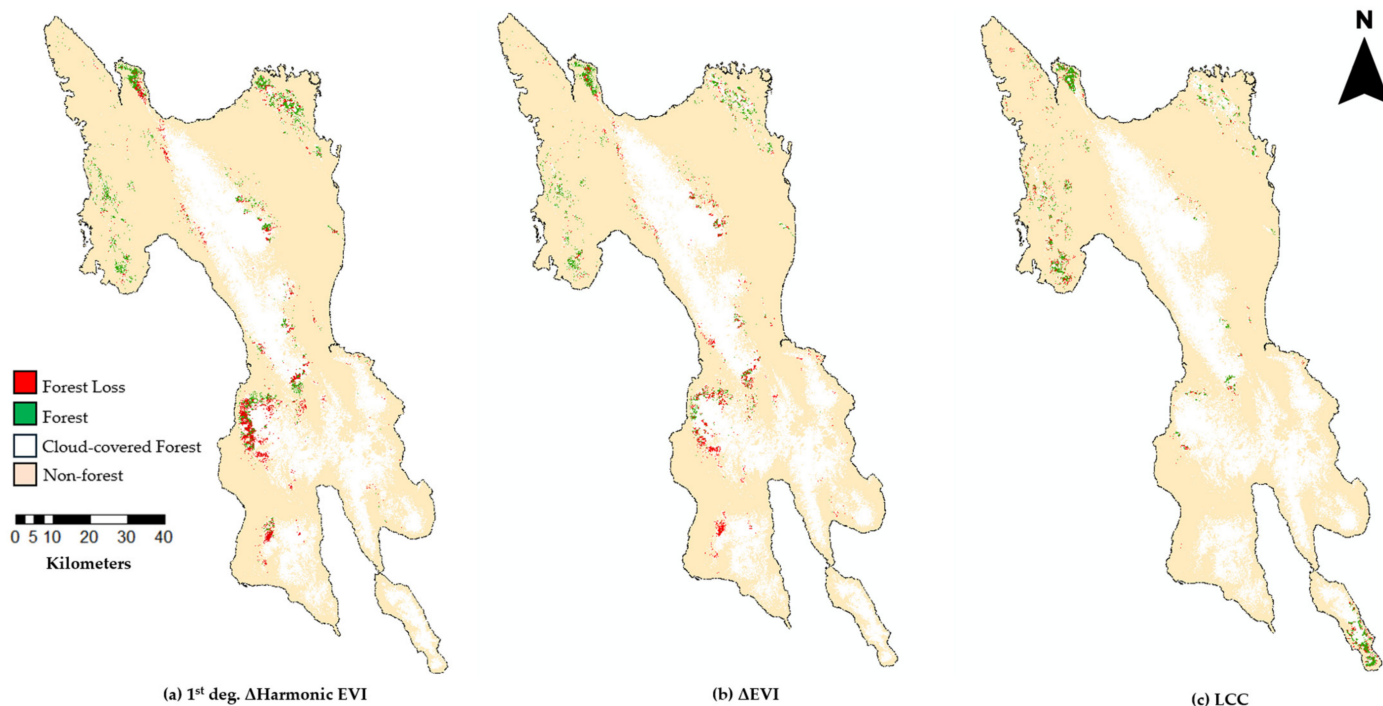
Figure 8. Forest Damage Map of the Leyte Region generated using (**a**) 1st-degree ΔHarmonic EVI using February 2022, and (**b**) ΔEVI for November 2021–February 2022 and (**c**) November 2021–February 2022 LCC.

The *ΔHarmonic* map showed a larger area coverage (Figure 8a) when compared to the ΔEVI (Figure 8b) and LCC map (Figure 8c). However, most forest areas are covered by clouds; thus, a method that minimizes the cloud cover effect is ideal.

The southern portion of the region closest to the typhoon shows the most damage, as illustrated in Figure 8. Damage can also be seen at the edges of the forest cover and near the coast, where trees are very vulnerable. To clearly observe the effect of typhoons, forest loss and terrain relationships must be further investigated (Section 2.2.6).

When comparing the forest loss observed on each map, *ΔHarmonic* (Figure 8a) showed a larger forest loss observation than the other two maps, owing to its sensitivity to disturbances and less susceptibility to cloud cover. The LCC map (Figure 8c) showed the lowest mapped forest loss area because it underestimated forest loss and had a low area coverage owing to cloud cover susceptibility.

A side-by-side comparison between the Forest Damage Map and PlanetScope's before- and after-typhoon delineated forest loss can be seen in Figure A2.

3.3. Investigating the Presence of Time Lag

In this study, a time lag was observed in the response of forests to typhoon disturbance. Figure 9a–d show the forest and forest losses in pixel count (1 pixel $\cong$ 0.0009 km^2) from the three *ΔHarmonic VI*s with the highest OA and from LCC. Forest loss increased from December 2021 to January 2022 and then decreased from January 2022 to February 2022. Subsequently, the forest area that experienced no loss decreased from December 2021 to January 2022 and then increased from January 2022 to February 2022. This same trend was also observed in most of the *ΔHarmonic VI* and *ΔVI* measurements. The trend showed

that there was a 1-month time delay in measuring the full effect of the typhoon on the forest region.
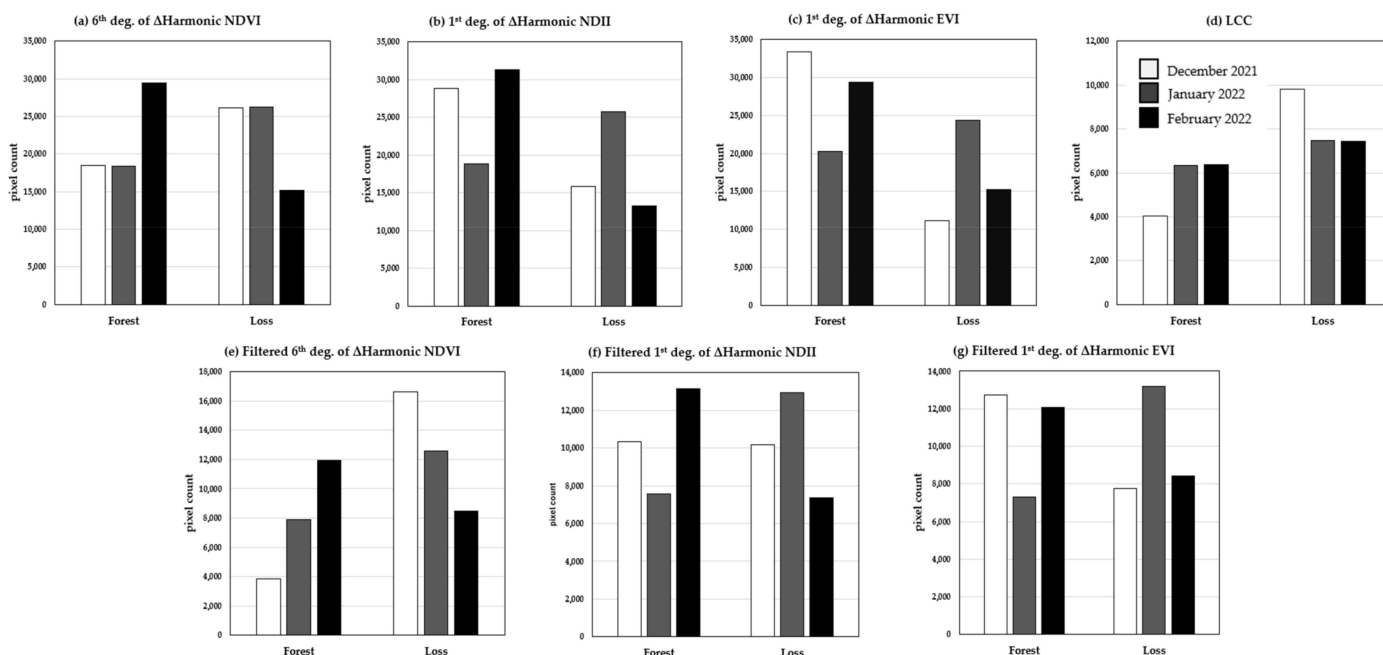
Figure 9. Pixel count of forest and forest loss area of the three ΔHarmonic VIs with the highest accuracy: (**a**) 6th-degree ΔHarmonic NDVI; (**b**) 1st-degree ΔHarmonic NDII; (**c**) 1st-degree ΔHarmonic EVI; (**d**) LCC; (**e**) filtered 6th-degree ΔHarmonic NDVI; (**f**) filtered 1st-degree ΔHarmonic NDII; (**g**) filtered 1st-degree ΔHarmonic EVI.

The December Landsat-derived HANTS VI image comprised two Landsat-8 OLI SR December images: 6 and 22 December 2021. Considering Typhoon Rai's date of occurrence, 14 December 2021, December HANTS VI was a combination of before- and after-typhoon images. To further investigate the effect of time lag, the effect of the pre-typhoon data that was present in December was filtered out in the pixel count analysis to clearly observe the time-lag effect after the typhoon hit.

Figure 9e–g show the result of removing the pre-typhoon data in December on the pixel count of the forest with and without loss. While NDVI showed no lag, NDII and EVI showed time lags. In ΔVI, the same pattern was also noted. Given that the NDVI has been shown to do poorly on dense vegetation, saturation may be the cause of the difference in trend seen with NDVI [44]. It peaked at a −45% threshold, requiring a wider range of percentage change in VI and overestimated forest loss areas in December, resulting in a low OA of 58.32% (filtered December data).

Knowing the time lag allows a better understanding of vegetation dynamics, and vegetation change measurements using VIs can be made accurately. To increase the ΔHarmonic EVI's accuracy in this study, the forest loss recorded in January and February was combined with the forest loss recorded in December. This was performed to account for the time-lag effect and monitor the behavior of the monthly detected forest loss. Merging was performed by first separating the forests with and without loss areas for each month pair. Then, for each group, the forests with/without a loss of area were merged by giving the later map higher priority than the preceding month in the merging method. Finally, the two groups were merged into one map by assigning the forest loss area the highest priority.

Figure 10 shows the result of merging the series of time-lag forest loss areas using the *ΔHarmonic VI*s with the best accuracy. OA increased as forest loss increased with each succeeding month, further proving the presence of a time lag. From merging, a better

1st-degree ΔHarmonic EVI damage map with a larger area coverage compared to Figure 8a with a similar OA was created, as shown in Figure 11.
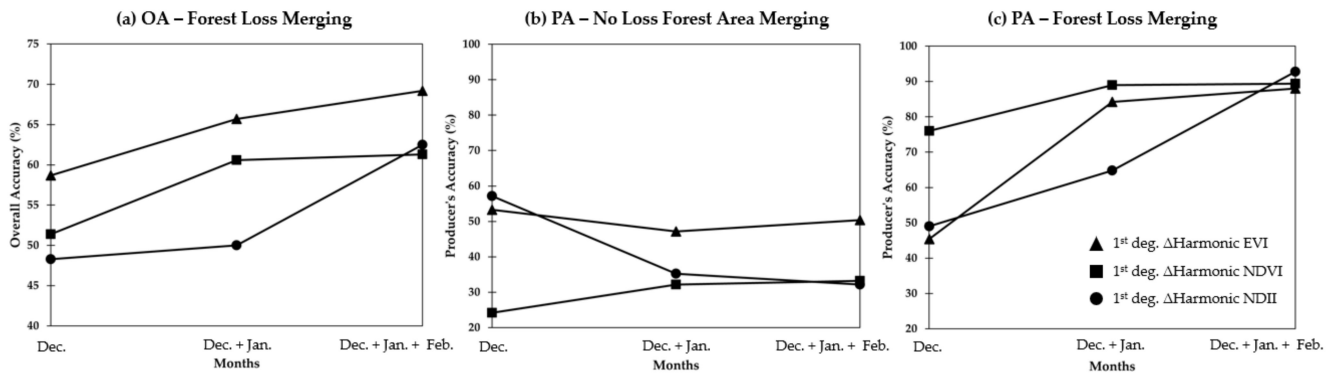

Figure 10. (**a**) Overall accuracy and (**b**) Producer's accuracy of no loss and (**c**) loss for 1st-degree ΔHarmonic EVI, NDVI, and NDII of merged forest loss areas from December 2021 to February 2022.
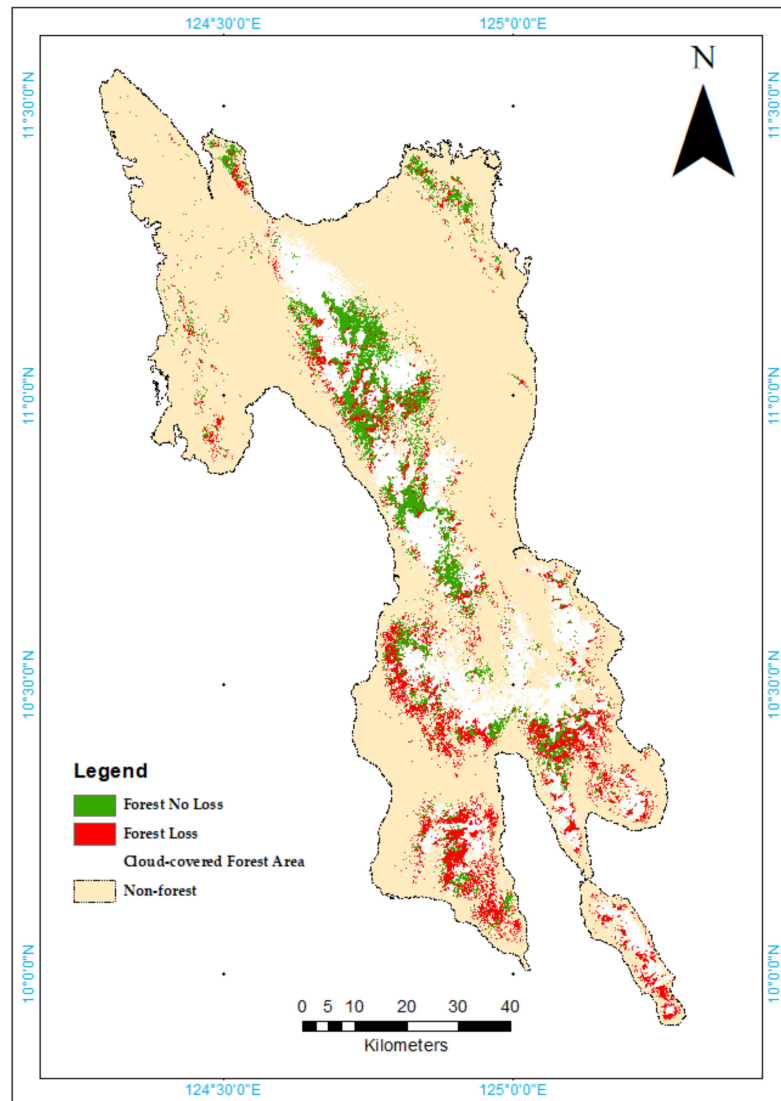
Figure 11. Forest Damage Map of the Leyte Region generated by merging the 1st-degree ΔHarmonic EVI December 2021 to February 2021 maps.

Figure 12 shows sample PlanetScope images of Hindang and Leyte before and after Typhoon Rai, with the Leyte Region Map showing the municipality's location. Yellow areas showed forest loss observed in the month of December 2021; orange areas showed forest loss observed both in the months of December 2021 and January 2022; and red areas showed forest loss observed for the three months—December 2021, January 2022, and February 2022. Figure 12 shows that the forest loss area changed over time, indicating that multiple dates after typhoon occurrence should be considered to better estimate the damage caused by typhoon disturbance.
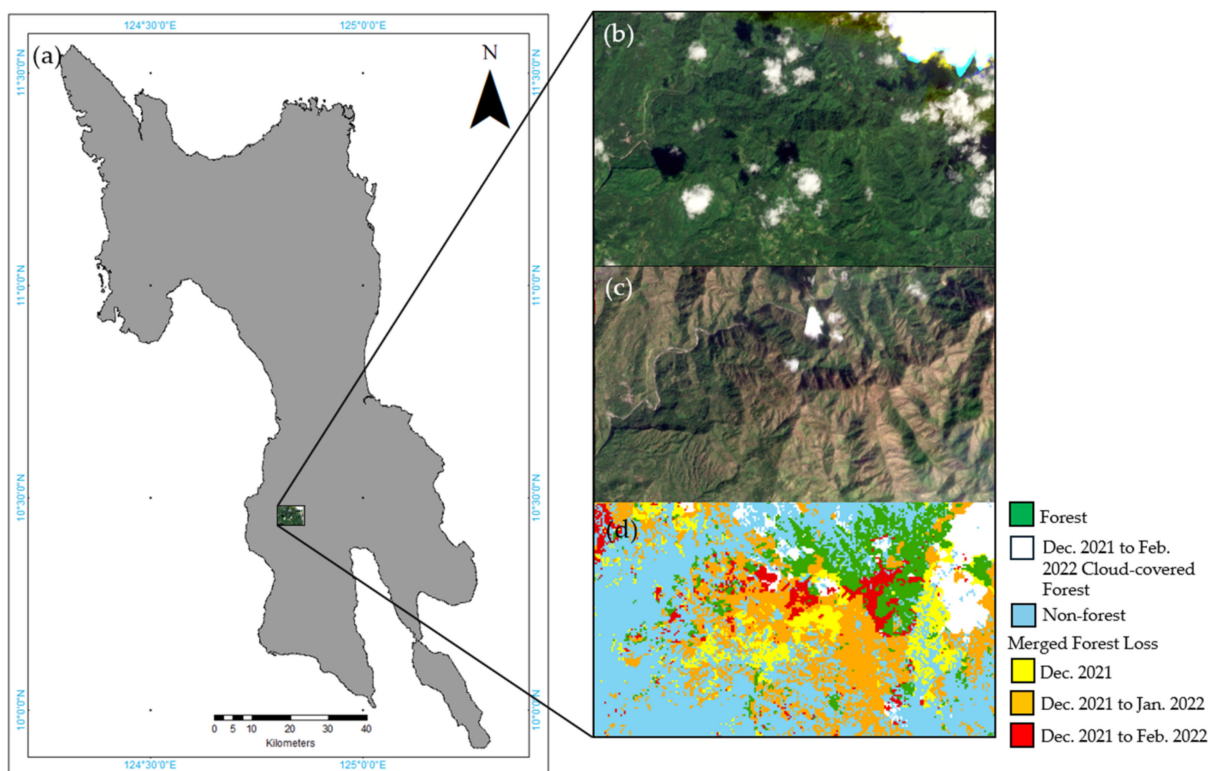

Figure 12. Comparison of (**a**) Hindang, Leyte (bounded by black box) PlanetScope images (**b**) before (20 November 2021) and (**c**) after typhoon Rai (12 January 2022), and (**d**) merged Forest Damage Map of 1st-degree ΔHarmonic EVI December 2021 to February 2022.

3.4. Determining Contributing Factors to Forest Damage

After generating the Forest Damage Map using HANTS, forest loss was compared with the Forest Damage Proximity Map and the region's topography. Figure 13 shows plots of the relationships between the measured damage through HANTS (Figure 8a), typhoon track, and topography.

Figure 13a shows that forest loss decreased as the distance from the typhoon increased. In Figure 13b, forest loss increased from 0° to 15° and then decreased from the 15° slope onward. Figure 13c shows that the forest loss increased from the 0° to 120° aspect, flattened from 120° to 240°, and then decreased from 240° to 360°. As shown in Figure 13d, forest loss increased from 0 m to 800 m, where it suddenly increased, and then decreased from 800 m to 1000 m.

With the plot, important topographic factors related to forest loss can be identified and provide valuable information to proper authorities for the careful planning of disaster preparedness and prevention.
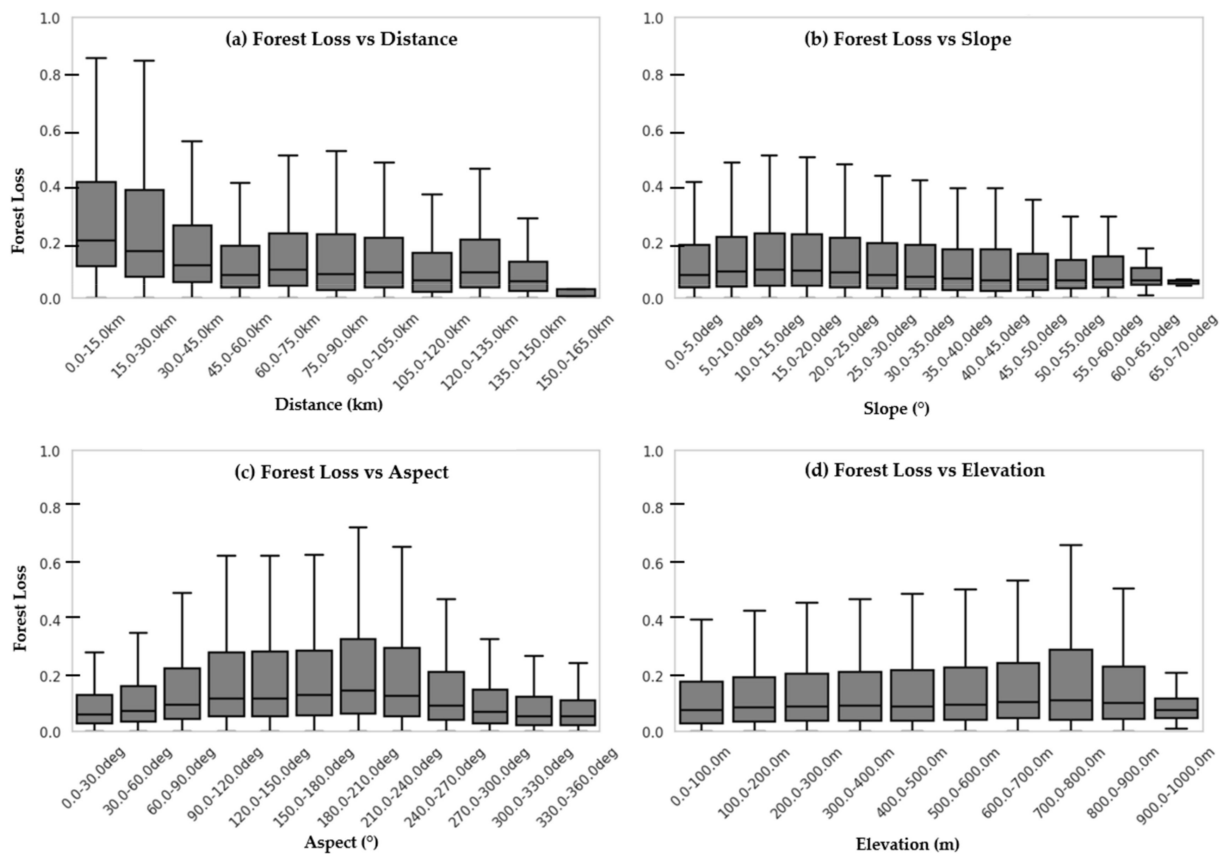
Figure 13. Forest loss compared to (**a**) proximity to typhoon, (**b**) slope (°), (**c**) aspect (°), and (**d**) elevation (m).

4. Discussion

4.1. Determining the Best Harmonic Degree and VI

4.1.1. Most Sensitive VI to Typhoon-Induced Forest Damage

From numerous *ΔHarmonic VI* comparisons with the validation data, the EVI showed the highest sensitivity among the VIs for forest loss. It showed better results than the NDVI, which agrees with a previous study regarding the application of both VIs to dense vegetation, such as forested areas [44]. Although the difference was small (2.20% at OA peaks), NDVI needed a higher threshold to distinguish forests with and without loss, showing less sensitivity.

The NDII was close to the EVI, with only a 0.10% difference in the OA peaks. This result conforms to those of previous studies, which suggested that the index is a good indicator for measuring vegetation disturbance [9,47,48].

Despite exhibiting the lowest OA peaks compared to the other VIs, GRVI also showed good accuracy on every degree of *ΔHarmonic VI*. In the Philippines, where there are only rainy and sunny seasons, it is unusual to find the use of an index that is normally used to determine the beginning of spring and autumn. However, as shown in this study, it can be a useful index for measuring typhoons because it is sensitive to typhoon-induced defoliation [49]. The index performed better than other VIs in some months when comparing *ΔHarmonic VI* and *ΔVI*. Another advantage of the GRVI is that it utilizes visible bands (Green and Red), unlike other VIs, which require bands beyond the visible range. This means that it is accessible because images in the visible range can be easily obtained.

4.1.2. Degree of Harmonic

The degree of harmonics with the highest accuracy across different VIs in this study was the 1st degree, followed by the 3rd degree of harmonic. This implies that only one

to three frequencies must be considered to describe the undisturbed phenology of the study area and obtain optimal results. This agrees with previous studies [22–24], wherein ideal vegetation phenology can be explained by the first three degrees, which are from vegetation growth and seasonal variation. Additionally, a more general model might be more appropriate given the size of the study area. The 6th degree of harmonics performed the worst among the considered degrees, which shows that the effect of the image's spatial resolution and other sources of disturbances did not significantly influence the signal for the undisturbed phenology. The only exception was in the case of the NDVI, where the 6th degree had a slightly better OA peak than the 1st degree. This might be due to the information from the additional frequencies compensating for the saturation issues that the index dealt with due to dense vegetation.

4.1.3. In Comparison With ΔVI and LCC Maps

LCC had the worst performance overall in the comparative analysis with *ΔHarmonic VI* and *ΔVI*. The LCC achieved its highest accuracy of 60.60% from the November 2021– February 2022 before- and after-typhoon images. It was 8.60% lower than *ΔHarmonic VI*'s peak of 69.20% with the 1st-Harmonic EVI and 7.00% lower than *ΔVI*'s highest at 67.60% with the change in NDVI between November 2021 and February 2022. The results showed that the *ΔHarmonic VI* method was comparable to the conventional methods used for forest damage assessment. It performed much better than the LCC.

Aside from having comparable results with *ΔVIs* and better results than LCC, the *ΔHarmonic VI* has several advantages.

First, the implementation of HANTS has been made simpler with the introduction of geospatial processing platforms like GEE. The time-series images and computational resources required by the method were provided by the platform. This method is also straightforward, making automation of the process possible. On the other hand, the LCC requires several rigorous processing steps and different datasets for implementation in the GEE. First, a reference image was required to create training points for classification. Often, the required reference image is not available on the platform, as in the reference used in this study. Then, a classifier must be produced using the reference image and the desired images to be processed. Depending on the accuracy of the classifier, supplementary data, which are sometimes not available on the platform, might be needed to increase its accuracy. To perform LCC detection, the LC image pair prior to and following the typhoon must be created. The LCC process is laborious and unlikely to be automated because it necessitates multiple recursions, stops, and checks.

Second, the accuracy of the LCC relies heavily on the spatial resolution of the data and the accuracy of land classification. However, its accuracy suffers when data with coarser resolutions are used. *ΔHarmonic VI* does not have these issues.

Third, *ΔHarmonic VI* only uses a single date image influenced by cloud cover, which is the *Observed VI*, as the *HANTS VI* can be generated from the harmonic model and is cloud-free. On the other hand, *ΔVI* and LCC need at least an image pair. These make *ΔHarmonic VI* not that susceptible to clouds. For regions like the Philippines, cloud cover is a significant hurdle in performing remote sensing analysis, and minimizing the effect of cloud cover would be very significant. Possessing a larger area coverage for damage assessment would also be of great impact on disaster response. Figure 8 illustrates this advantage. Figure 9 shows the difference in pixel count between *ΔHarmonic VI* and LCC. Additionally, Table 3 shows the pixel count and area difference of *ΔHarmonic VI* and *ΔVI* to see the advantage of the proposed method in numbers.

Fourth, historical damage maps can be used to provide context for the causes of forest damage seen in recent events and can be used to properly evaluate and prepare for future typhoon events. Because *ΔHarmonic VI* utilizes historical data through HANTS, a Forest Damage Map from any typhoon disturbance that occured at any point in time can be generated as long as it is within the range of the harmonic series. This makes this study

applicable when typhoon damage occurs frequently and makes the comparison of typhoon damage at different times of occurrence possible.

Table 3. Coverage difference between ΔHarmonic VI and ΔVI.

Method	Total Pixel Count		
	December	**January**	**February**
ΔHarmonic EVI	796,573	420,546	219,350
ΔEVI	501,586	327,268	157,893
diff.	294,987	93,278	61,457
Area diff.[1] (km^2)	265.49	83.95	55.31

[1] Conversion: 1 pixel = 0.03 × 0.03 km (Landsat-8 Spatial Resolution).

Finally, as *ΔHarmonic VI* contains continuous data that computes the percentage change in a vegetation index, it has the potential to assess damage by severity. This can also be said of the remaining forests. *ΔHarmonic VI*, which utilizes vegetation indices, can indicate forest degradation or growth. However, as discrete data, LCCs can only indicate the presence or absence of forests.

4.2. Different Contributing Factors to Forest Damage

From Figures 8 and 11, areas south of the Leyte Region have a high susceptibility to damage as they are near the typhoon path. Regions near the coast and at forest cover edges also showed damage from typhoons. To further understand the damage observed, the map was compared to the topography and typhoon track, and the results are shown in Figure 13.

The distance plot (Figure 13a) shows peaks in the first 30 km because these areas are near the typhoon. Peaks were also observed at the 90th and 120th km intervals. However, it is difficult to determine the cause of these peaks because multiple factors could affect them, such as terrain and forest cover. Mountains are dispersed throughout the Leyte Region, despite the region's abundance of level coastal areas.

In the case of the slope (Figure 13b), forest loss increased from 0° to 15° and then declined throughout the succeeding slopes. This conforms to the results of other studies [12,13].

Regarding the aspect (Figure 13c), the slope of the terrain and the direction, rotation, and position of the typhoon must all be considered. Figure 12c, which shows the separation between the damaged and non-damaged areas, demonstrates the effects of both aspect and slope. Because the Philippines is in the Northern Hemisphere, typhoons rotate counterclockwise and usually move from west to east. So, the area located on the right side of the typhoon path was expected to experience stronger winds due to its rotation and the addition of the typhoon's speed. Thus, slopes north of Typhoon Rai's path facing east will receive stronger winds than slopes facing west in this study because the typhoon's path was westward; the opposite is true for areas south of the typhoon. Therefore, aspect, in combination with slope, is an important factor in these types of analyses. In the plot, there was a peak in forest loss at around 90°–120°. This was expected, as Typhoon Rai, based on Figure 2, passed to the south of the Leyte Region, causing the slopes facing east to catch the full strength of the typhoon wind. There is also a dip at approximately 240–270°, as these slopes face the opposite direction of the wind direction.

Finally, an upward trend between forest loss and elevation (Figure 13d) was clearly observed. Forest loss steadily increased from 0 to 700 m in elevation, followed by a sudden rise at 700–800 m. Subsequently, it declined from 800 m onward. This sudden peak may be due to the exposed forest patches on top of the hills, making the area more susceptible to further losses [13].

To improve the applicability of the method and determine which factors contribute more to the forest loss, it is recommended to use detailed validation data in which grading the changes before and after the typhoon to severity could be possible. This would

improve the identification of damage hotspots and make the estimations more accurate and quantifiable. A corresponding, current, and accurate map of the forest cover should be added to this.

5. Conclusions

This study demonstrates the applicability of HANTS to Landsat-8 and PlanetScope images for mapping typhoon-induced forest damage. It showed that the method is comparable to the conventional ways used in forest assessment, with comparable accuracy versus *ΔVI* and LCC. It also showed several advantages of the method compared to *ΔVI* and LCC.

Using the method, a Forest Damage Map of the Leyte Region was created through *ΔHarmonic VI* and was used to identify damage hotspots. This approach can be used to utilize past data to assess the present and plan for the future, as this study showed proof of the advantage of this method in using historical data.

This study was also able to show the presence of time lag and contributing factors such as the typhoon track and terrain in relation to the mapped forest loss due to the typhoon.

Overall, the approach using *ΔHarmonic VI* was successful in measuring forest loss caused by a typhoon. This study achieves its primary objectives. With the use of just one set of data, which was easily accessible to the public, and implementation through GEE, it has been shown that the method is effective, simple, and transferable. The Government and local sectors can easily adapt this method and use it to guide them in creating effective forest management plans, forming appropriate responses to typhoons towards a more resilient forest and, in turn, building a more resilient, disaster-ready community.
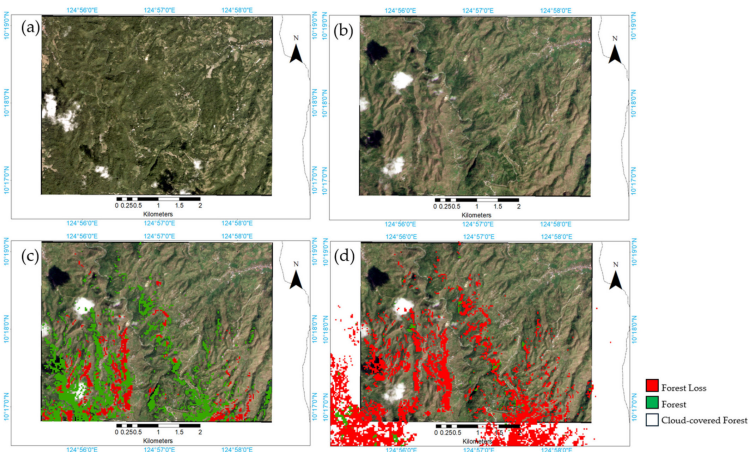
Appendix A

(a)   (b)   (c)   (d)

Figure A1. PlanetScope's images of Maasin City, Leyte, (**a**) before (25 October 2021) and (**b**) after Typhoon Rai (19 December 2021). (**c**) Delineated changes between before and after images. (**d**) Image bounds intersected with forest cover map and mosaicked with delineated damage areas.
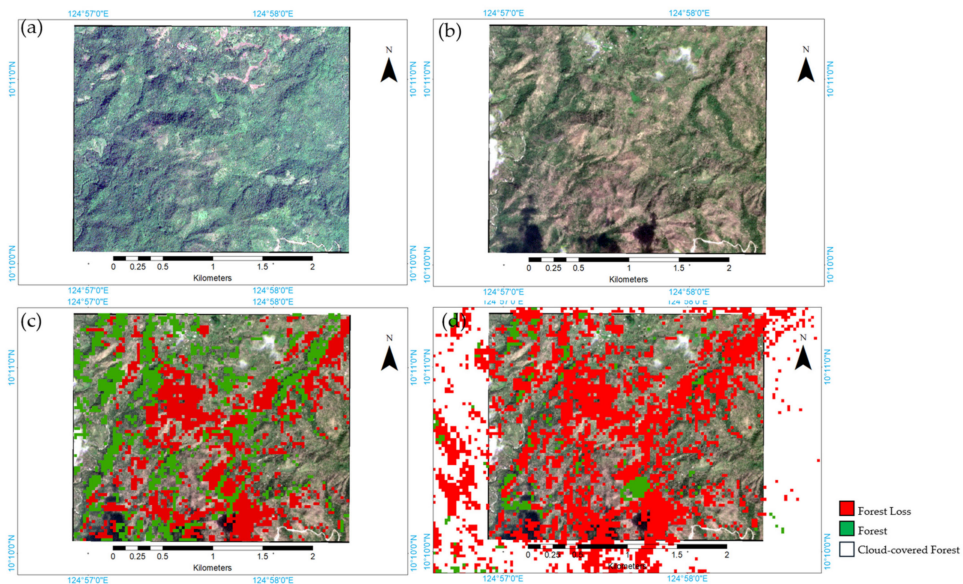
San Juan, Leyte, Philippines
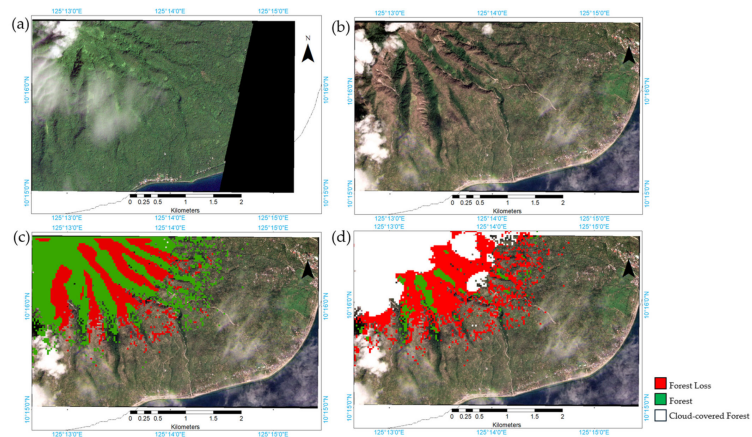
Tomas Oppus, Leyte, Philippines

Malitbog, Leyte, Philippines

Figure A2. Side-by-side comparison (**a**) before and (**b**) after Typhoon Rai hit the selected areas in Leyte Region as seen from PlanetScope with the (**c**) delineated forest and forest loss through visual interpretation and land classification and (**d**) forest and forest loss mapped using HANTS method. Dates of registration of the images were from 21 to 26 March 2024.

References

1. The World Bank. *Agriculture, Forestry, and Fishing, Value Added (% of GDP)—Philippines. Economic Policy & Debt: National Accounts: Shares of GDP and Other*; The World Bank Group: Washington, DC, USA, 2022.
2. Profor World Bank Group. Understanding the Role of Forests in Enhancing Livelihoods and Climate Resilience: Case Studies in the Philippines. In *How Forests Enhance Livelihoods and Climate Resilience*; Program on Forests (PROFOR): Washington, DC, USA, 2017; pp. 1–4.
3. Wiebe, P.C.; Zhunusova, E.; Lippe, M.; Velasco, R.F.; Günter, S. What is the Contribution of Forest-related Income to Rural Livelihood Strategies in the Philippines' Remaining Forested Landscapes? *For. Policy Econ.* **2022**, *135*, 102658. [CrossRef]
4. Chechina, M.; Neveux, Y.; Parkins, J.R.; Hamann, A. Balancing Conservation and Livelihoods: A Study of Forest-dependent Communities in the Philippines. *Conserv. Soc.* **2018**, *16*, 420–430. [CrossRef]
5. van Hensbergen, H.; Cedergren, J. *Forest-Related Disasters—Three Case Studies and Lessons for Management of Extreme Events*; Forestry Working Paper No. 17; FAO: Rome, Italy, 2020; pp. 7–26. [CrossRef]
6. Xiao, L.; Robinson, M.; O'Connor, M. Woodland's Role in Natural Flood Management: Evidence from Catchment Studies in Britain and Ireland. *Sci. Total. Environ.* **2022**, *813*, 151877. [CrossRef] [PubMed]
7. Del Rosario, E.D.; Ramos, B.T.; Jalad, R.B.; Rabonza, G.J. *Situational Reports Regarding Preparedness Measures and Effects for Typhoons*; NDRRMC: Quezon City, Philippines, 2009–2023.
8. Aosier, B.; Kaneko, M.; Takada, M. Evaluation of the forest damage by typhoon using remote sensing technique. In Proceedings of the 2007 IEEE International Geoscience and Remote Sensing Symposium, Barcelona, Spain, 23–28 July 2007. [CrossRef]
9. Wang, W.; Qu, J.J.; Hao, X.; Liu, Y.; Stanturf, J.A. Post-Hurricane Forest Damage Assessment Using Satellite Remote Sensing. *Agric. For. Meteorol.* **2010**, *150*, 122–132. [CrossRef]
10. Dong, G.; Liu, Z.; Du, G. Assessment of vegetation damage by three typhoons (Bavi, Maysak, and Haishen) in Northeast China in 2020. *Nat. Hazards* **2022**, *150*, 2883–2899. [CrossRef]
11. Peereman, J.; Hogan, J.A.; Lin, T.-C. Assessing Typhoon-Induced Canopy Damage Using Vegetation Indices in the Fushan Experimental Forest, Taiwan. *Remote Sens.* **2020**, *12*, 1654. [CrossRef]
12. Zhang, X.; Jiao, H.; Chen, G.; Shen, J.; Huang, Z.; Luo, H. Forest Damage by Super Typhoon Rammasun and Post-Disturbance Recovery Using Landsat Imagery and the Machine-Learning Method. *Remote Sens.* **2022**, *14*, 3826. [CrossRef]
13. Chen, X.; Avtar, R.; Umarhadi, D.A.; Louw, A.S.; Shrivastava, S.; Yunus, A.P.; Khedher, K.M.; Takemi, T.; Shibata, H. Post-Typhoon Forest Damage Estimation Using Multiple Vegetation Indices and Machine Learning Models. *Weather Clim. Extrem* **2022**, *38*, 100494. [CrossRef]
14. Zhang, X.; Chen, G.; Cai, L.; Jiao, H.; Hua, J.; Luo, X.; Wei, X. Impact Assessments of Typhoon Lekima on Forest Damages in Subtropical China Using Machine Learning Methods and Landsat 8 OLI Imagery. *Sustainability* **2021**, *13*, 4893. [CrossRef]
15. Cui, L.; Shi, J. Temporal and spatial response of vegetation NDVI to temperature and precipitation in eastern China. *J. Geogr. Sci.* **2010**, *20*, 163–176. [CrossRef]
16. Chuai, X.W.; Huang, X.J.; Wang, W.J.; Bao, G. NDVI, temperature and precipitation changes and their relationships with different vegetation types during 1998–2007 in Inner Mongolia, China. *Int. J. Climatol.* **2012**, *33*, 1696–1706. [CrossRef]
17. Xu, Y.; Shen, Y. Reconstruction of the Land Surface Temperature Time Series Using Harmonic Analysis. *Comput. Geosci.* **2013**, *61*, 126–132. [CrossRef]
18. Azzali, S.; Menenti, M. *Fourier Analysis of Temporal NDVI in the Southern African and American Continents*; DLO Winand Staring Centre: Wageningen, The Netherlands, 1996; pp. 108–151.
19. Wilson, B.T.; Knight, J.F.; McRoberts, R.E. Harmonic Regression of Landsat Time Series for Modeling Attributes from National Forest Inventory Data. *ISPRS J. Photogramm. Remote Sens.* **2018**, *137*, 29–46. [CrossRef]
20. Malamiri, H.R.G.; Zare, H.; Rousta, I.; Olafsson, H.; Verdiguier, E.I.; Zhang, H.; Mushore, T.D. Comparison of Harmonic Analysis of Time Series (HANTS) and Multi-Singular Spectrum Analysis (M-SSA) in Reconstruction of Long-Gap Missing Data in NDVI Time Series. *Remote Sens.* **2020**, *12*, 2720. [CrossRef]
21. Sajadi, P.; Sang, Y.; Gholamnia, M.; Bonafoni, S.; Brocca, L.; Pradhan, B.; Singh, A. Performance Evaluation of Long NDVI Timeseries from AVHRR, MODIS, and Landsat Sensors over Landslide-Prone Locations in Qinghai-Tibetan Plateau. *Remote Sens.* **2021**, *13*, 3172. [CrossRef]
22. Jakubauskas, M.E.; Legates, D.R.; Kastens, J.H. Crop identification using harmonic analysis of time-series AVHRR NDVI data. *Comput. Electron. Agric.* **2002**, *37*, 127–139. [CrossRef]
23. Geerken, R.A. An algorithm to classify and monitor seasonal variations in vegetation phenologies and their inter-annual change. *ISPRS J. Photogramm. Remote Sens.* **2009**, *64*, 422–431. [CrossRef]
24. Philipp, M.; Wegmann, M.; Kübert-Flock, C. Quantifying the Response of German Forests to Drought Events via Satellite Imagery. *Remote Sens.* **2021**, *13*, 1845. [CrossRef]
25. Philippine Statistics Authority. Highlights of the Region VIII (Eastern Visayas) Population 2020 Census of Population and Housing (2020 CPH). 2020. Available online: https://psa.gov.ph/content/highlights-region-viii-eastern-visayas-population-2020-census-population-and-housing-2020 (accessed on 29 March 2024).
26. European Commission. Digital Observatory for Protected Areas (DOPA) Explorer: Mindanao-Eastern Visayas Rain Forests. Available online: https://dopa-explorer.jrc.ec.europa.eu/ecoregion/40129 (accessed on 24 June 2024).

27. National Hurricane Center and Central Pacific Hurricane Center. Annual 2021 Tropical Cyclones Report. Available online: https://www.ncei.noaa.gov/access/monitoring/monthly-report/tropical-cyclones/202113 (accessed on 24 March 2024).

28. Reuters. Philippine Death Toll from Its Strongest Typhoon of the Year Tops 400. 2021. Available online: https://www.reuters.com/markets/commodities/philippine-death-toll-its-strongest-typhoon-year-tops-400-2021-12-31/ (accessed on 29 March 2024).

29. United States Geological Survey (USGS). Landsat 8 Operational Land Imager (OLI) and Thermal Infrared Sensor (TIRS). Available online: https://www.usgs.gov/core-science-systems/nli/landsat/landsat-8 (accessed on 29 March 2024).

30. Planet Team. Planet Application Program Interface: In Space for Life on Earth. San Francisco, CA. 2022. Available online: https://api.planet.com (accessed on 24 March 2024).

31. Planet Team. PlanetScope: Constellation and Sensor Overview. Available online: https://developers.planet.com/docs/data/planetscope/ (accessed on 24 June 2024).

32. Francini, S.; McRoberts, R.; Giannetti, F.; Mencucci, M.; Marchetti, M.; Mugnozza, G.; Chirici, G. Near-real time forest change detection using PlanetScope imagery. *Eur. J. Remote Sens.* **2020**, *53*, 233–244. [CrossRef]

33. Chung, M.; Kim, Y. Object-based wildfire damage assessment using PlanetScope images. In Proceedings of the 40th Asian Conference on Remote Sensing, Daejeon, Republic of Korea, 14–18 October 2019.

34. Chung, M.; Han, Y.; Kim, Y. A framework for unsupervised wildfire damage assessment using VHR and satellite images with PlanetScope data. *Remote Sens.* **2020**, *12*, 3835. [CrossRef]

35. Gasparovic, M.; Klobucar, D.; Gasparovic, I. Automatic Forest degradation monitoring by remote sensing methods and Copernicus data. *Int. Arch. Photogramm. Remote Sens. Spat. Inf. Sci.* **2022**, *XLIII-B3-2022*, 611–616. Available online: https://isprs-archives.copernicus.org/articles/XLIII-B3-2022/611/2022/ (accessed on 29 March 2024). [CrossRef]

36. Dalagnol, R.; Wagner, F.; Galvao, L.; Braga, D.; Osborn, F.; Sagang, L.; Bispo, P.; Payne, M.; Silva, C., Jr.; Favrichon, S.; et al. Mapping tropical forest degradation with deep learning and Planet NICFI data. *Remote Sens. Environ.* **2023**, *298*, 113798. [CrossRef]

37. Carter, G.; Wagner, F.; Dalagnol, R.; Roberts, S.; Ritz, A.; Saatchi, S. Detection of forest disturbance across California using deep learning on PlanetScope imagery. *Front. Remote Sens.* **2024**, *5*, 1409400. [CrossRef]

38. Japan Aerospace Exploration Agency (JAXA). Advanced Land Observing Satellite (ALOS) Digital Surface Model (DSM) Global Dataset. Approximate Resolution 30 m. Available online: https://www.eorc.jaxa.jp/ALOS/en/dataset/aw3d30/aw3d30_e.htm (accessed on 24 March 2024).

39. National Mapping and Resource Information Authority (NAMRIA). Land Use and Land Cover Map. Geoportal Philippines. Available online: http://geoportal.gov.ph (accessed on 3 March 2024).

40. Keenan, R.; Reams, G.; Achard, F.; de Freitas, J.; Grainger, A.; Lindquist, E. Dynamics of Global Forest Area: Results from the FAO Global Forest Resources Assessment 2015. *For. Ecol. Manag.* **2015**, *352*, 9–20. [CrossRef]

41. Rousseeuw, P.J.; Hubert, M. Robust statistics for outlier detection. *Wiley Interdiscip. Rev. Data Min. Knowl. Discov.* **2011**, *1*, 73–79. [CrossRef]

42. Piragnolo, M.; Pirotti, F.; Zanrosso, C.; Lingua, E.; Grigolato, S. Responding to Large-Scale Forest Damage in an Alpine Environment with Remote Sensing, Machine Learning, and Web-GIS. *Remote Sens.* **2021**, *13*, 1541. [CrossRef]

43. Chang, C.-T.; Wang, S.-F.; Vadeboncoeur, M.A.; Lin, T.-C. Relating Vegetation Dynamics to Temperature and Precipitation at Monthly and Annual Timescales in Taiwan Using MODIS Vegetation Indices. *Int. J. Remote Sens.* **2014**, *35*, 598–620. [CrossRef]

44. Huete, A.R.; Didan, K.; Miura, T.; Rodriguez, E.P.; Gao, X.; Ferreira, L.G. Overview of the Radiometric and Biophysical Performance of the MODIS Vegetation Indices. *Remote Sens. Environ.* **2002**, *83*, 195–213. [CrossRef]

45. Wang, M.; Xu, H. Remote Sensing-Based Assessment of Vegetation Damage by a Strong Typhoon (Meranti) in Xiamen Island, China. *Nat. Hazards* **2018**, *93*, 1231–1249. [CrossRef]

46. Wang, F.; D'Sa, E.J. Potential of MODIS EVI in Identifying Hurricane Disturbance to Coastal Vegetation in the Northern Gulf of Mexico. *Remote Sens.* **2010**, *2*, 1–18. [CrossRef]

47. Townsend, P.A.; Singh, A.; Foster, J.R.; Rehberg, N.J.; Kingdon, C.C.; Eshleman, K.N.; Seagle, S.W. A General Landsat Model to Predict Canopy Defoliation in Broadleaf Deciduous Forests. *Remote Sens. Environ.* **2012**, *119*, 255–265. [CrossRef]

48. Zhang, K.; Thapa, B.; Ross, M.; Gann, D. Remote Sensing of Seasonal Changes and Disturbances in Mangrove Forest: A Case Study from South Florida. *Ecosphere* **2016**, *7*, e01366. [CrossRef]

49. Motohka, T.; Nasahara, K.N.; Tsuchida, S. Applicability of Green-Red Vegetation Index for Remote Sensing of Vegetation Phenology. *Remote Sens.* **2010**, *2*, 2369–2387. [CrossRef]

50. Menenti, M.; Azzali, S.; Verhoef, W.; van Swol, R. Mapping Agroecological Aones and Time lag in Vegetation Growth by means of Fourier Analysis of Time series of NDVI images. *Adv. Space Res.* **1993**, *5*, 233–237. [CrossRef]

51. Verhoef, W. Application of harmonic analysis of NDVI time series (HANTS). In *Fourier Analysis of Temporal NDVI in the Southern African and American Continents*; Azzali, S., Menenti, M., Eds.; Report 108; DLO Winand Staring Centre: Wageningen, The Netherlands, 1996; pp. 19–24.

52. Furukawa, F.; Morimoto, J.; Yoshimura, N.; Kaneko, M. Comparison of Conventional Change Detection Methodologies Using High-Resolution Imagery to Find Forest Damage Caused by Typhoons. *Remote Sens.* **2020**, *12*, 3242. [CrossRef]